

# The NGC 5253 star cluster system. I. Standard modelling and infrared-excess sources

Richard de Grijs,<sup>1,2,3\*</sup> Peter Anders,<sup>1</sup> Erik Zackrisson<sup>4</sup> and Göran Östlin<sup>4</sup>

<sup>1</sup> *Kauli Institute for Astronomy and Astrophysics, Peking University, Yi He Yuan Lu 5, Hai Dian District, Beijing 100871, China*

<sup>2</sup> *Department of Astronomy and Space Science, Kyung Hee University, Yongin-shi, Kyungki-do 449-701, Republic of Korea*

<sup>3</sup> *2012 Selby Fellow, Australian Academy of Science*

<sup>4</sup> *Department of Astronomy, Stockholm University, Oscar Klein Centre, AlbaNova, Stockholm SE-106 91, Sweden*

Received date; accepted date

## ABSTRACT

Using high-resolution *Hubble Space Telescope* data, we reexamine the fundamental properties (ages, masses and extinction values) of the rich star cluster population in the dwarf starburst galaxy NGC 5253. The gain in resolution compared to previous studies is of order a factor of two in both spatial dimensions, while our accessible wavelength range transcends previous studies by incorporation of both near-ultraviolet and near-infrared (IR) passbands. We apply spectral synthesis treatments based on two different simple stellar population model suites to our set of medium-, broad-band and  $H\alpha$  images to gain an improved physical understanding of the IR-excess flux found for a subset of young clusters (30 of 149). With the caveat that our models are based on fully sampled stellar mass functions, the NGC 5253 cluster population is dominated by a significant number of relatively low-mass ( $M_{cl} \lesssim$  a few  $10^4 M_{\odot}$ ) objects with ages ranging from a few  $\times 10^6$  to a few  $\times 10^7$  yr, which is in excellent agreement with the starburst age of the host galaxy. The IR-excess clusters are almost all found in this young age range and have masses of up to a few  $\times 10^4 M_{\odot}$ . The IR excess in the relatively low-mass NGC 5253 clusters is most likely caused by a combination of stochastic sampling effects and colour variations due to the presence of either luminous red or pre-main-sequence stars. We also find a small number of intermediate-age ( $\sim 1$  Gyr-old),  $\sim 10^5 M_{\odot}$  clusters, as well as up to a dozen massive,  $\sim 10$  Gyr-old globular clusters. Their presence supports the notion that NGC 5253 is a very active galaxy that has undergone multiple episodes of star cluster formation.

**Key words:** methods: data analysis – stars: luminosity function, mass function – galaxies: starburst – galaxies: star clusters: general – infrared: galaxies

## 1 INTRODUCTION

### 1.1 Choice of target

NGC 5253, a metal-poor blue compact dwarf galaxy in the Centaurus A group (Karachentsev et al. 2007), hosts an extremely young starburst. At the fortuitously close distance of 3.13 Mpc (Davidge 2007; 1 arcsec corresponds to 16 pc), the galaxy has been the target of a large number of observational programmes spanning a range of wavelengths, from X-rays to the radio domain (e.g., Rieke, Lebofsky & Walker 1988; Caldwell & Phillips 1989; Martin & Kennicutt 1995; Freedman et al. 2001; Cresci, Vanzì & Sauvage 2005; Martín-Hernández, Schaerer & Sauvage 2005; López-Sánchez et al. 2007, 2011).

The metallicity of NGC 5253, approximately 0.2–0.4  $Z_{\odot}$  (Kobulnicky & Skillman 1995; Kobulnicky et al. 1999; López-Sánchez et al. 2011), is relatively constant across the galaxy, except for a few areas exhibiting higher-than-average nitrogen abundances (Walsh & Roy 1989; Kobulnicky et al. 1997; López-Sánchez et al. 2007; López-Sánchez & Esteban 2010a,b; Monreal-Ibero et al. 2010) and a possible slight helium enrichment (Campbell, Terlevich & Melnick 1986; López-Sánchez et al. 2007). This low metallicity, combined with the galaxy’s relatively small dimensions ( $\sim 5 \times 2$  arcmin<sup>2</sup>  $\simeq 4.6 \times 1.8$  kpc<sup>2</sup> major/minor axis extents) and low mass ( $\sim 2\text{--}5 \times 10^9 M_{\odot}$ ; Bottinelli et al. 1972; Turner, Beck & Hurt 1997), render its starburst component an excellent analogue to galaxies in their early formation phases, while its proximity makes it ideal for studies of the many bright, young stellar clusters (YSCs; e.g., Gonzalez-Riestra, Rego & Zamorano 1987; Caldwell & Phillips 1989; Calzetti et al.

\* E-mail: grijs@pku.edu.cn

1997; Harris et al. 2004; Vanzi & Sauvage 2004; Cresci et al. 2005; Martín-Hernández et al. 2005; Harbeck, Gallagher & Crnojević 2012).

In fact, based on ultraviolet (UV) *Hubble Space Telescope (HST)*/Space Telescope Imaging Spectrometer (STIS) spectroscopy of the YSCs and diffuse background light in the main body of the galaxy, Tremonti et al. (2001) suggested that star clusters may have been forming continuously, and subsequently dissolve on  $\sim 10$ – $20$  Myr timescales (based on arguments related to tidal effects worked out in detail in Kim, Morris & Lee 1999; a process since coined cluster ‘infant mortality’), thus dispersing their stars into the field star population.

## 1.2 Starburst characteristics

The galaxy’s H $\alpha$  morphology (Martin 1998; Calzetti et al. 2004; Meurer et al. 2006) shows that the inner core is currently undergoing intense star formation and is, in fact, one of the youngest starbursts known (van den Bergh 1980; Moorwood & Glass 1982; Rieke et al. 1988; Caldwell & Phillips 1989; Calzetti et al. 1997; McQuinn et al. 2010a,b). The active starburst is confined to the inner 60 pc (Calzetti et al. 1997, 1999; Tremonti et al. 2001); age estimates for the starburst duration in this region are  $< 1 \times 10^7$  yr, and more likely a few  $\times 10^6$  yr, assuming a burst-like formation history for the diffuse stellar population in the disc (Walsh & Roy 1989; Rieke et al. 1988; Tremonti et al. 2001). These estimates are based on weak [Fe II] emission, strong Br $\gamma$  emission, a lack of significant (non-thermal) synchrotron emission from supernova remnants (Beck et al. 1996), the presence of Wolf–Rayet stars (Campbell et al. 1986; Kobulnicky et al. 1997; Schaerer et al. 1997; López-Sánchez et al. 2007; López-Sánchez & Esteban 2010a,b; Monreal-Ibero et al. 2010) and weak  $2\mu\text{m}$  emission, implying only a small contribution of giants and supergiants, which thus provides a rough upper age limit.

In two very detailed studies of the galaxy’s central starburst region, Calzetti et al. (1997, 1999) showed that the UV emission is dominated by a 3–4 Myr old, relatively small star cluster, NGC 5253-4 (Meurer et al. 1995). On the other hand, a dust-enshrouded ( $A_V = 9$ – $35$  mag) very young central cluster (2–2.7 Myr old), NGC 5253-5, is responsible for most of the nuclear region’s ionization (Tremonti et al. 2001; Cresci et al. 2005). At radio wavelengths, Turner et al. (1998, 2000) derive ionization potentials driven by large numbers (200–1000) of O-type stars, which they interpret to imply that very large clusters are the preferred mode of star formation in the central regions of the galaxy.

## 1.3 Current context

It is thus clear that the galaxy’s star and star cluster formation history is highly complex. Despite the plethora of existing, detailed studies, many of the salient details of the galaxy’s evolution remain open-ended. This realization is perhaps mostly driven by the object’s proximity, which allows us to probe the star-forming environment in significantly greater detail than in more distant starbursts. On the other hand, NGC 5253’s proximity also offers us the key advantage of it having been observed repeatedly across the full observable wavelength range.

Nevertheless, where the stellar component has been subject to detailed scrutiny, most studies have either focussed on careful, mostly spectroscopic studies of a few objects at a time, or systematic exploration of the galaxy’s full extent but based on relatively simple approaches. This is particularly so for its star cluster population. Previous statistical studies have relied on straightforward application of simple stellar population (SSP) analysis based on optical broad-band data (e.g., Harris et al. 2004; Cresci et al. 2005; Harbeck et al. 2012). However, in recent years, theory and computational approaches have made significant advances.

In this paper, we go significantly beyond previous studies of the NGC 5253 star cluster population in a number of complementary ways. First, although we still use primarily (medium- and) broad-band imaging observations, we base our results on the highest-achievable spatial resolution from the near-UV (NUV) to the near-infrared (NIR) regimes. The gain in resolution compared to previous studies is of order a factor of two in both spatial dimensions, while our accessible wavelength range transcends previous studies by incorporation of the crucial NUV and NIR passbands (which will allow us to at least partially break the age–metallicity and age–extinction degeneracies). Where relevant, we also refer to H $\alpha$  emission-line results to further reduce the uncertainties.

Second, we focus specifically on one aspect of extragalactic star cluster populations where we take full advantage of the observational gains, i.e., the importance and origin of a red or IR excess in the spectral-energy distributions (SEDs) of a relatively low-mass cluster population such as that in NGC 5253. To address this aspect, we do not need to have access to a statistically complete sample of star clusters down to the lowest detection limits enabled by the observations’ worst signal-to-noise ratio (S/N).

This paper is organized as follows. In Section 2 we discuss the observational data which form the basis of our analysis, as well as our data reduction approach. The analysis methods adopted are outlined in Section 3, while we discuss the robustness of the results and perform a comparison in Section 4. We offer a preliminary discussion of the effects of stochasticity in the stellar mass function separately, in Section 5, and provide an overview of the physical state of the NGC 5253 cluster population in Section 6. Finally, we summarize and conclude the paper in Section 7.

This is the first article in a series of three. In Paper II (P. Anders et al., in prep.), we will present a detailed theoretical investigation of the effects of stochastic sampling on cluster age and mass determinations based on adopting fully sampled stellar mass functions using our own SSP models and analysis approach (cf. Section 3). In Paper III (R. de Grijs et al., in prep.), we will apply these insights to the data set analysed here, to explore in detail to which extent our results are affected by biases owing to stochastic sampling of the clusters’ mass functions. The present paper is meant to establish the baseline for this body of work.

## 2 HUBBLE SPACE TELESCOPE OBSERVATIONS AND DATA REDUCTION

### 2.1 Data and basic reduction

We mined the *HST* Data Archive for available medium-/broad-band and H $\alpha$  observations of NGC 5253 obtained

with its main optical and NIR cameras, i.e., the Advanced Camera for Surveys (ACS), the Wide-Field and Planetary Camera-2 (WFPC2) and the Near-Infrared Camera and Multi-Object Spectrometer (NICMOS). Since we had selected our target galaxy based on the availability of a large number of high-resolution *HST* data sets spanning the longest possible wavelength range, we could make a careful selection of the best possible data sets to reach our science goals. Table 1 includes details of the final set of observations used, which were selected to achieve the best possible combination of spatial resolution (aimed at reducing contamination by neighbouring sources), S/N (for which we initially used exposure time as a proxy) and extensive, continuous wavelength coverage.

## 2.2 Object selection

We used the ACS/HRC data in the F330W, F435W, F550M and F814W filters as basis for the final orientation of all observations. This implies that we rotated, scaled and aligned all other images to the position, scale and orientation of the ACS/HRC data using the IRAF/STSDAS tasks<sup>1</sup> ROTATE, MAGNIFY, and IMALIGN, respectively, using a selection of conspicuous sources common to each frame as guides. We checked that our image manipulation did not affect the reliability of the integrated flux measurements of our sample of candidate star clusters. The final image size of the set of aligned images is  $1169 \times 1138$  ACS/HRC pixels,<sup>2</sup> corresponding to  $32.73 \times 28.45$  arcsec<sup>2</sup> ( $\sim 500 \times 430$  pc<sup>2</sup>).

The standard deviations ( $\sigma_{\text{sky}}$ ) of the number of counts in seemingly empty sections in all images were established to ascertain a ‘sky’ background count for each filter. Multiples of this background count were used as thresholds above which the numbers of ‘real’ sources in both the F550M and F814W ACS/HRC filters were calculated, using the IDL<sup>3</sup> FIND task. We did not force our detection routine to constrain the sources’ roundness or sharpness, in order to be as inclusive as possible. The most suitable thresholds for source inclusion, at  $4\sigma_{\text{sky}}$  (see below for justification), were 0.7 and 1.5 counts s<sup>-1</sup> (270 and 248 source detections) for the F550M and F814W filters, respectively. In all passbands, the number of detections initially decreases rapidly with increasing threshold value. This is an indication that our ‘source’ detections are noise-dominated in the low-threshold regime. Where the rapid decline slows down to a more moderate rate, our detections become dominated by ‘real’ objects (either stars, clusters or cluster candidates, or real intensity variations in the background field: for an example, see fig. 3 of Barker et al. 2008). In the remainder of this paper we will

only consider the objects in the ‘source-dominated’ domain, with fluxes in excess of the relevant  $4\sigma_{\text{sky}}$  threshold.

We subsequently employed a cross-identification procedure to determine how many sources coincided with intensity peaks within 1.4 pixels of each other in the F550M⊗F814W HRC filter combination (i.e., allowing for 1-pixel mismatches in both spatial directions). In our next step, we applied a Gauss-fitting routine in IDL to each candidate cluster. We also determined the best-fitting Gaussian profiles for some 10–12 isolated, star-like sources in all filters (where the number of objects available for this purpose depended on the S/N of the observations and the typical stellar spectra) and thus obtained observational stellar Gaussian  $\sigma_G$  (size) values for all filters. The Gaussian stellar widths in the F550M HRC band (the filter we used for our size selection) were found to be best represented by a Gaussian profile of  $\sigma_G = 1.1$  pixels. Any candidate cluster with  $\sigma_{G, F550M} \leq 1.1$  pixels was considered most likely to be a star (or – if much smaller than 1 pixel – an artefact either of the detector or caused by cosmic rays) and was consequently discarded. We applied a conservative clipping criterion so as not to reject some marginally extended sources. These steps resulted in rejection of 88 objects from the original F550M source list and led to a working sample containing 182 extended cluster candidates.

Their size distribution is shown in Fig. 1, where we also show the linear cluster sizes after deconvolution of the observed  $\sigma_G$  and the intrinsic size of the point-spread function (PSF). Our (candidate) cluster sample is characterized by a peak at sizes close to that of the PSF, while the most extended cluster candidate has  $\sigma_G = 3.4$  pixels (equivalent to 1.36 pc after PSF deconvolution). Our sample is insensitive to stellar associations because of the selection criteria adopted. We will discuss the implications of the cluster size distribution (as well as the insets in Fig. 1) in Section 6.4. In a final step, we confirmed that our procedure is robust with respect to misidentifications of genuine clusters as point sources (stars): only a few ( $\lesssim 5$ ) per cent of the objects that were rejected based on the Gaussian size estimates were brighter than the tip of the red giant branch (TRGB) magnitude at the distance of NGC 5253, where we used the most recent calibration based on observations of  $\omega$  Centauri,  $M_I^{\text{TRGB}} = -4.04 \pm 0.12$  mag (Bellazzini et al. 2001, 2004).

We note that although realistic cluster luminosity profiles may well deviate from the simple Gaussian profile adopted here, its consistent and systematic application to our observations allows us to differentiate accurately between objects of different sizes, irrespective of their true profiles, provided that the intrinsic profiles of the individual objects do not differ too much from object to object (although one should realize that stochastic sampling effects may invalidate this assumption; see below). In Fig. 2 we show the distribution of our candidate cluster sample across the face of the NGC 5253 common field in the ACS/HRC F550M filter.<sup>4</sup> The main differences between our current sample selection and that of Cresci et al. (2005) – the most recent detailed statistical study of the NGC 5253 cluster system – are owing to the higher-resolution images we used as the

<sup>1</sup> The Image Reduction and Analysis Facility (IRAF) is distributed by the National Optical Astronomy Observatories, which is operated by the Association of Universities for Research in Astronomy, Inc., under cooperative agreement with the U.S. National Science Foundation. STSDAS, the Space Telescope Science Data Analysis System, contains tasks complementary to the existing IRAF tasks. We used Version 3.6 (November 2006) for the data reduction performed in this paper.

<sup>2</sup> The ACS/HRC pixels are rectangular and subtend  $0.028 \times 0.025$  arcsec<sup>2</sup> each.

<sup>3</sup> The Interactive Data Language (IDL) is licensed by Research Systems Inc., of Boulder, CO, USA.

<sup>4</sup> For a movie including all high-resolution images and object identifications, see <http://kiaa.pku.edu.cn/~grijs/ngc5253.mov>.

**Table 1.** *HST* observations used for the analysis in this paper.

Filter	Camera	Chip	Exposures (s)	Total exp. time (s)	Proposal ID	PI	Photometric corr. factor (unit)
F330W	ACS	HRC	3 × 449	1347	10609	Vacca	1.0 ( $\sigma_{\text{HRC}}$ )
F435W	ACS	HRC	4 × 150	600	10609	Vacca	1.1 ( $\sigma_{\text{HRC}}$ )
F547M	WFPC2	WF	2 × 200, 2 × 600	1600	6524	Calzetti	1.6 ( $\sigma_{\text{WFC}}$ )
F550M	ACS	HRC	4 × 200	800	10609	Vacca	1.0 ( $\sigma_{\text{HRC}}$ )
F555W	ACS	WFC	4 × 600	2400	10765	Zezas	1.0 ( $\sigma_{\text{WFC}}$ )
F606W	WFPC2	PC	500	500	5479	Malkan	2.0 ( $\sigma_{\text{HRC}}$ )
F658N	ACS	HRC	240	240	10609	Vacca	1.0 ( $\sigma_{\text{HRC}}$ )
F814W	ACS	HRC	4 × 92	368	10609	Vacca	1.25 ( $\sigma_{\text{HRC}}$ )
F110W	NICMOS	NIC2	4 × 23.97	95.86	7219	Scoville	1.2 ( $\sigma_{\text{WFC}}$ )
F160W	NICMOS	NIC2	4 × 23.97	95.86	7219	Scoville	1.1 ( $\sigma_{\text{WFC}}$ )
F222M	NICMOS	NIC2	4 × 63.95	255.80	7219	Scoville	1.15 ( $\sigma_{\text{WFC}}$ )

Note: The three-digit numbers in the filter names represent their effective wavelengths in nanometres; the final digits indicate the filter type: N = narrow, M = medium, W = wide.

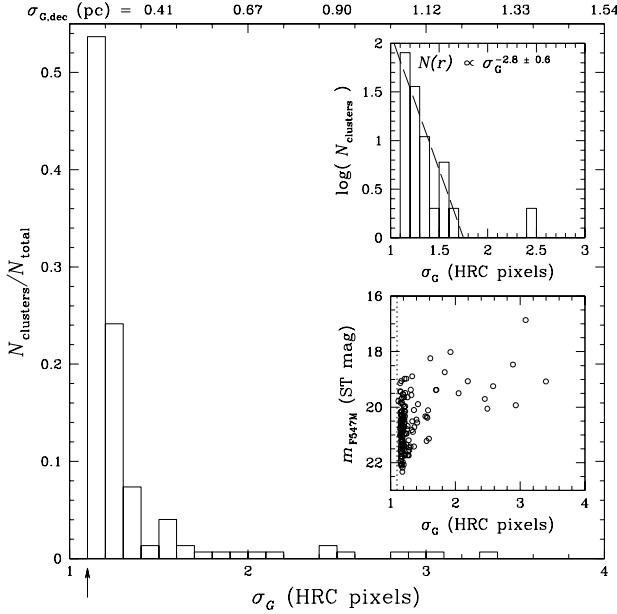


**Figure 1.** Gaussian size distribution of the extended star cluster candidates in our sample (as fraction of the total sample). The arrow indicates our minimum size cut-off, corresponding to the  $\sigma_{\text{G}}$  of point sources. The top axis shows the linear cluster sizes after deconvolution of the observed  $\sigma_{\text{G}}$  and the intrinsic size of the PSF. The insets show the size distribution (*top*) in logarithmic units, combined with the best-fitting power-law function (dashed line, defined by the proportionality given) and (*bottom*) as a function of F547M magnitude (see Section 6.4 for discussion). The vertical dotted line indicates the ACS/HRC PSF size.

basis for our object identification, thus reducing crowding effects. As a result, we find slightly fewer cluster candidates in the galaxy’s main body; some of the sources identified by Cresci et al. (2005) as ‘clusters’ are unresolved (and likely stars) in our images (with  $\sigma_{\text{G}} \leq 2.65$  pc, corresponding to a PSF-deconvolved size of  $\sigma_{\text{G,dec}} \leq 2.4$  pc).

### 2.3 Photometry

Our custom-written IDL aperture photometry task uses source radii and sky annuli *individualized* for each cluster candidate. The adopted radii and annuli were based on Gaussian stellar size measurements ( $\sigma_{\text{G}}$ ) obtained in the F550M filter. We applied a correction factor as a function of filter/instrument to correct for different intrinsic PSF sizes (see the final column in Table 1), based on determination of the best-fitting Gaussian profiles for the 10–12 isolated, star-like sources in all filters we used for our size cuts in Section 2.2. We used the F550M HRC and F555W ACS/Wide Field Camera (WFC) images as our basis for the determination of source and sky annuli because of their high resolution and good S/N: in images with HRC (or similar, e.g., WFPC2/PC) resolution, we used a source aperture radius of  $4 \times [\sigma_{\text{F550M}} \times \text{HRC correction factor}]$ , and 4 and  $6 \times [\sigma_{\text{F550M}} \times \text{HRC correction factor}]$  for the inner and outer sky annuli (in pixels), respectively. For the other images, characterized by poorer resolution, the relevant numbers were 3, 3.5 and  $5 \times [\sigma_{\text{F555W}} \times \text{WFC correction factor}]$ , respectively, again expressed in pixel units (the WFC chips are characterized by a pixel size of 0.049 arcsec). The units in the final column of Table 1 corresponding to  $\sigma_{\text{HRC}}$  and  $\sigma_{\text{WFC}}$  refer to  $\sigma_{\text{F550M}}$  and  $\sigma_{\text{F555W}}$ , respectively.

This choice of apertures and their scaling with the objects’ measured sizes was based on extensive tests in which we inspected the stellar radial profiles, to identify where the object profiles generally disappear into the background noise. Specifically, we carefully checked the profiles of all candidate clusters, for all filters and detectors, to verify that our source radii were chosen conservatively and sufficiently far out so as not to exclude any genuine source flux with respect to the general background level (i.e., well in excess of the radii where the radial profiles disappear into the background noise). We also checked that the background annuli were chosen appropriately and not dominated by neighbouring sources. Finally, we checked that the background level was generally flat (within the photometric uncertainties and the statistical noise) so that small differences among the radii used to define the background annuli as a function of filter would not cause artificial offsets in flux, and hence lead to colour differences.

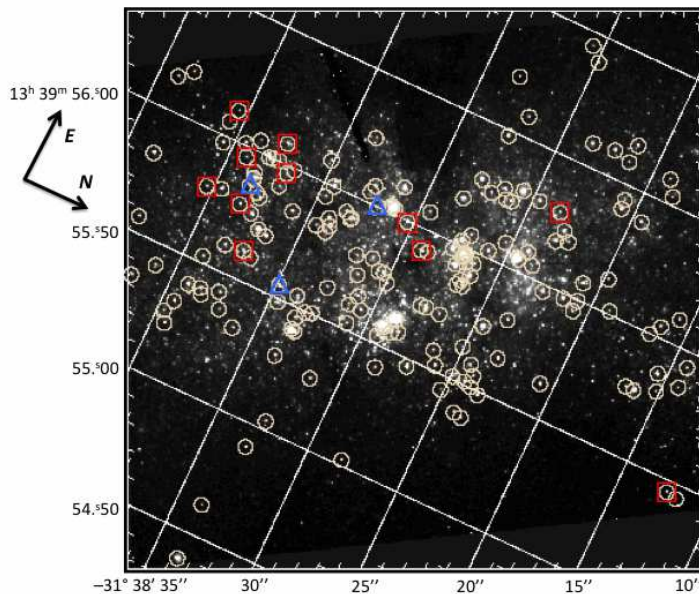


**Figure 2.** NGC 5253 field of view in common of all observations and source selection discussed in this paper, overlaid on the ACS/HRC F550M image. Red squares: Age  $t \simeq 10^{10}$  yr; blue triangles:  $t \simeq 10^9$  yr (for a discussion of the clusters’ spatial distribution as a function of age, see Section 6.1).

Fig. 3 shows a typical example of the level of photometric accuracy attainable with individualized apertures compared to the use of fixed apertures. For this example, we employed source apertures of 8 pixels (in the detector’s native system) and background annuli between 8 and 12 pixels for our ACS-based fixed-aperture photometry. For the F547M WFPC2/WF and the NICMOS images, we used equivalent radii of 12, 12 and 15 pixels, again in the respective detectors’ native systems. The photometric data points in the different panels only include those objects for which the individualized apertures were smaller than or equal to the sizes of our fixed apertures, so that a direct one-to-one comparison is possible. The mean differences in the sense ( $m_{\text{indiv. ap.}} - m_{\text{fixed ap.}}$ ), as well as the standard deviations of these difference distributions are included in each of the panels for the relevant instrument/filter combination. It is clear that the correspondence between our individualized aperture photometry and that obtained from using fixed apertures (chosen so that most sources would have most of their flux recorded) is tight. The scatter increases for the lower-resolution and lower-S/N images, although the mean difference remains small, particularly within the associated uncertainties.

For the size cut-offs ( $1.1\sigma_G$ ) in the HRC F550M and the WFC F555W filters, the annuli adopted in this study correspond to deconvolved linear sizes of 2.35, 2.35 and 3.50 pc, and 2.45, 3.85 and 4.10 pc, respectively. The resulting instrumental magnitudes of the 182 ‘clusters’ for which our tasks could obtain reliable photometry (with photometric uncertainties of  $< 0.3$  mag in at least 7 filters) were adjusted for their zero-point offsets (determined from the PHOTFLAM and PHOTZPT header keywords of the *HST* observations, thus resulting in photometry in the ST mag system). This sample forms the basis of our analysis in Sections 4 and 5. We will make the full photometric data tables of all 182

cluster candidates available in Paper III, upon completion of our detailed investigation of the effects of stochasticity in the clusters’ stellar mass functions.

Note that because of the extended nature of our objects (which was, after all, a key selection criterion), we could not apply PSF photometry or simple aperture corrections (but see, e.g., Harris et al. 2004; Annibali et al. 2011); the latter would require uncertain assumptions about, e.g., the underlying source profile (cf. Anders, Gieles & de Grijs 2006) as well as the degree of mass segregation within the clusters. The rationale for such an approach is to attempt to obtain the full flux of a given object. Particularly for the lower-luminosity, lower-mass objects, the effects of stochastic sampling would likely introduce additional uncertainties if adopting a generic underlying radial profile. On the other hand, adopting an aperture correction to large radii based on the profile and colours in a restricted region relatively close to a cluster’s core may give rise to additional colour- and age-dependent uncertainties in the derived total fluxes owing to the effects of stellar mass segregation. Instead, we opted to use a hybrid method: our aperture sizes were variable, i.e., based on the measured cluster sizes and designed such that our output photometry included the full flux contribution from all objects.<sup>5</sup>

In addition, our integrated SEDs are dominated by the highest-luminosity (inner) regions of the clusters (we checked that any contribution from potentially missed flux in the outer regions is negligible), so that the resulting parameters do not strongly depend on our aperture photom-

<sup>5</sup> In a sense, whether or not one should (or even could) use aperture corrections to recover the fluxes of extended objects is a philosophical issue. In this paper, we decided to adopt the lessons learnt from the results of Anders et al. (2006) and choose source apertures based on the objects’ size measurements.

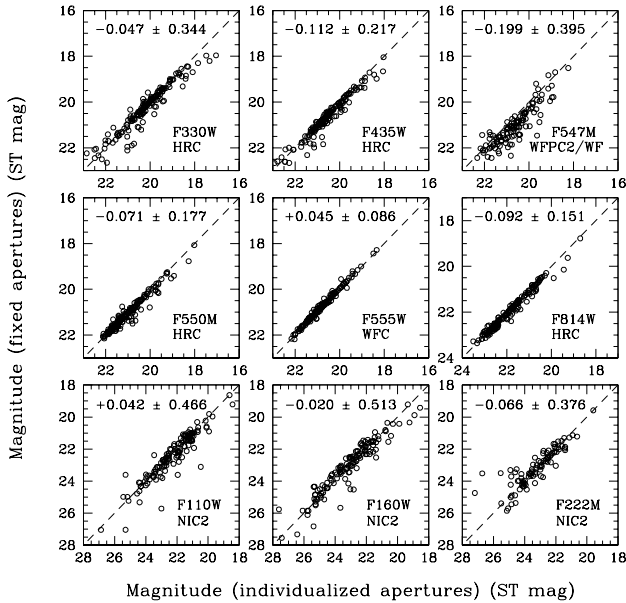


**Figure 3.** Comparison of aperture photometry based on our individualized apertures and that from the use of fixed apertures. For this example, we employed source apertures of 8 pixels (in the detector’s native system) and background annuli between 8 and 12 pixels for our ACS-based fixed-aperture photometry. For the F547M WFPC2/WF and the NICMOS images, we used equivalent radii of 12, 12 and 15 pixels, again in the respective detectors’ native systems. The photometric data points in the different panels only include those objects for which the individualized apertures were smaller than or equal to the sizes of our fixed apertures, so that a direct one-to-one comparison is possible. The mean differences in the sense ( $m_{\text{indiv. ap.}} - m_{\text{fixed ap.}}$ ), as well as the standard deviations of these difference distributions are included in each of the panels for the relevant instrument/filter combination (also indicated). The dashed lines indicate the loci of equality.

etry approach (see also Section 4.4). Finally, the majority of our sample clusters are sufficiently isolated that our approach is not severely affected by the effects of crowding; this is supported by inspection of the growth curves of the dozen sample clusters in the most crowded regions. Ultimately, the main advantage of our hybrid approach is that it is simple and requires few, if any, assumptions that may introduce additional uncertainties.

Fig. 4 compares the resulting photometry with that published by Harris et al. (2004). The latter authors published ST magnitudes for 33 objects they identified as clusters, 25 of which are also included in our cluster sample. We note that the overall agreement between both data sets is reasonable, although in half a dozen cases there are significant offsets. The latter occur particularly for the brighter objects in the F547M filter.

Harris et al. (2004) discuss the best approach to obtaining reliable photometry in the crowded environment of NGC 5253, which is additionally affected by significant background variations. They conclude that PSF-like photometry is inappropriate under these conditions, and that aperture corrections depend sensitively on the underlying luminosity profile adopted. They settled on achieving a balance between

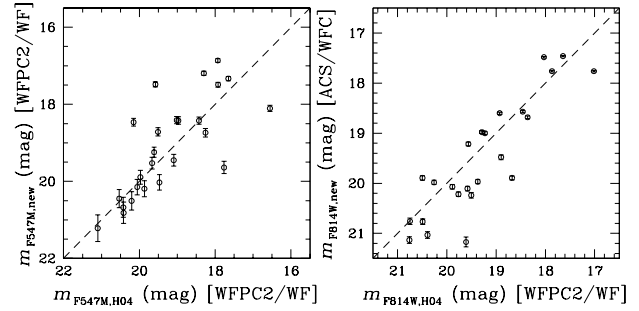


**Figure 4.** Comparison of our photometry using a hybrid approach (indicated by the subscript ‘new’) with that of Harris et al. (2004), based on aperture corrections appropriate for point sources (referred to as H04), both in the ST mag system.

the systematic errors imposed by small apertures and the random errors inherent to adopting large apertures by selecting an intermediate aperture size of 5 pixels (radius). They then attempt to correct for the clusters’ extended profiles by adopting a 0.1 mag, 5-pixel aperture correction appropriate for point sources, but they caution that it is likely that there remains a systematic error in the photometry because of the clusters’ non-spherical, extended morphologies. In this context, the offsets in the F547M photometry between our determinations and those of Harris et al. (2004) can be understood fairly easily. For the brighter, extended sources in particular, the 5-pixel apertures they adopted are too small to encompass the full source fluxes, thus leading to underestimated luminosities (fainter magnitudes) on average. This is evident from inspection of Fig. 4, particularly for objects with  $m_{F5547M} \lesssim 20$  mag (in both sets of photometric measurements). In addition, two bright objects ( $m_{F5547M,H04} \lesssim 18$  mag) have brighter magnitudes in the data set of Harris et al. (2004) than determined by us. These objects are found in the most crowded regions of the galaxy, where their extended profiles overlap with neighbouring objects. On balance, we prefer to use our own newly determined photometry, because this attempts to include and correct for the effects of non-sphericity and spatial extent. We also point out that a comparison of our photometry based on different apertures (shown in Fig. 3) indicates that our measurements are internally consistent.

The scatter in the F814W photometry is somewhat larger than that for the F547M data, which is most likely caused by the difference in resolution between the cameras used in the presence of fairly crowded fields. Lower-resolution observations, such as the WFPC2 data of Harris et al. (2004), are more significantly affected by close neighbours (‘blending’) than the higher-resolution ACS data we use in this paper. In addition, there is a small systematic offset towards brighter magnitudes for our photometry compared to the Harris et al. (2004) data set, which is most likely caused by their underestimated aperture corrections for point sources.

In Section 3 we analyse our cluster photometry based on the objects’ colours. In essence, we use a poor man’s approach to cluster spectroscopy based on the clusters’ broadband SEDs.

### 3 SED ANALYSIS

We base our SED analysis on two of the current-best, most up-to-date SSP model suites available, specifically the Yggdrasil models (Section 3.2) and the GALEV models (Section 3.3). Both sets of models are based on different, modern isochrones and independently developed spectral synthesis codes, which have all been extensively validated. Although there are currently at least a handful of suitable SSP model suites to choose from, the two model sets we adopted are most appropriate in the context of the present paper, since a number of our co-authors are actively involved in their development. This offers the key advantage that we fully understand the basic underlying assumptions and essential physical inputs, which we summarize in detail in this section.

#### 3.1 General model assumptions

For a one-to-one comparison between the observed and model SEDs, we assumed that star clusters are coeval (single-burst) stellar populations characterized by a Kroupa (2001) IMF. This IMF is characterized by a lower cut-off mass of  $0.15 M_{\odot}$ , whereas the upper-mass cut-off ranges between  $\sim 66$  and  $\sim 76 M_{\odot}$ , and is determined by the mass coverage of the Padova isochrones (i.e., Marigo et al. 2008) for a given metallicity, e.g., the upper mass cut-off for  $Z = 0.004$  (0.008) is  $68.07$  ( $70.35$ )  $M_{\odot}$ . The theoretical stellar libraries are from Lejeune et al. (1997, 1998) for a broad range of metallicities.

The current versions of both sets of models include the important thermally pulsing asymptotic-giant-branch (TP-AGB) evolutionary phase. At ages from  $\sim 100$  Myr to  $\sim 1$  Gyr, TP-AGB stars account for 25 to 40 per cent of the bolometric light, and for 50 to 60 per cent of the  $K$ -band emission of SSPs (see Charlot 1996; Schulz et al. 2002). The effect of including the TP-AGB phase results in redder colours for SSPs with ages between  $\sim 10^8$  and  $10^9$  yr, with the strongest effect (up to  $\gtrsim 1$  mag) in  $(V - K)$  for solar metallicity, and in  $(V - I)$  for  $Z \geq 0.5 Z_{\odot}$ . Shorter-wavelength colours and lower-metallicity SSPs are less affected.

The models predict the contributions to the combined SED of both the stars and the ambient, photo-ionized gas owing to the presence of young massive stars. The photo-ionized gas contributes both to the continuum and to specific emission lines, thus directly affecting the integrated broadband fluxes of YSCs. Anders & Fritze-v. Alvensleben (2003) and Adamo et al. (2010b) showed that nebular emission non-negligibly affects cluster SEDs during the first 10–15 Myr of their evolution. Although this contribution reduces after 6 Myr, at least for shorter (bluer) wavelengths, it remains significant in the NIR regime up to  $\sim 20$  Myr (depending on metallicity).

#### 3.2 Yggdrasil models and IR-excess analysis

*Model-specific details.* The primary approach we adopted for our analysis in this paper uses the most up-to-date Yggdrasil spectral synthesis models (Zackrisson et al. 2011). The latter are based on Padova-AGB SSPs from the Starburst99 spectral synthesis code (Leitherer et al. 1999; Vazquez & Leitherer 2005). For our application to the NGC 5253 cluster system, we adopted metallicities of  $Z = 0.004$  and  $0.008$

(where  $Z_{\odot} = 0.019$ ). Adopting the Calzetti et al. (2000) attenuation law, which is characterized by total-to-selective absorption  $R_V = 4.05$  and most appropriate for use in starburst environments, we created a grid of models including  $0.0 \leq E(B - V) \leq 3.0$  mag for each age step.

For the gaseous contribution, our models employed standard HII region values as input parameters to CLOUDY (version 90.05; Ferland et al. 1998), i.e., a hydrogen gas density of  $10^2 \text{ cm}^{-3}$ , a filling factor of 0.01 and a covering factor of unity (no leakage of ionizing photons, so that – for instance – all Lyman continuum photons contribute to ionizing the gas). In addition, we assumed that the metallicities of the stars and gas in a given cluster are identical.

*Parameter determination.* We used a least-squares fit to estimate, for each cluster, the best-fitting model (expressed in magnitudes; see, e.g., Adamo et al. 2010a) and calculated the associated  $Q$  value (or  $\chi^2$  probability function: models with  $Q \gtrsim 0.1$  are good, while  $Q > 0.001$  is still marginally acceptable; Press et al. 1992), as well as the reduced  $\chi^2_{\nu} = \chi^2/\nu$ , where  $\nu = N - m - 1$  is the number of degrees of freedom given  $N$  data points and  $m$  fit parameters. Here,  $N$  refers to the number of filters and  $m = 2$ , i.e., we obtain best fits of the age and extinction ( $m = 2$ ) and a scaled mass of each cluster for fixed metallicity. The resulting 68 per cent confidence limits on the determination of the cluster parameters were based on the prescription of Lampton, Margon & Bowyer (1976). Adamo et al. (2010a,b, 2011a,b) used the spectral synthesis models of Marigo et al. (2008) to validate their results.

Adamo et al. (2010a) discovered that several young clusters in the luminous blue compact galaxy (BCG) Haro 11 have a flux excess in the  $I$ ,  $H$  and  $K_s$  bands. Inclusion of those filters in the fit resulted in significant residuals and a clear overestimation of the cluster age. Given the starburst nature of NGC 5253, we expected that at least some of the galaxy’s YSCs might be affected by a similar red excess.

Therefore, we produced three series of  $\chi^2$  minimizations, i.e., one including all available data points from the NUV regime (F330W) to the F222M filter, a second excluding F110W, F160W and F222M (i.e., from the NUV to the  $I$  band), and a third which also excluded the  $I$  band (leaving the range up to the F606W filter’s effective wavelength). Our initial analysis showed that the latter filter selection did not produce any improvement to the fit (in the  $\chi^2$  sense) and this filter selection leaves too few constraints on the resulting cluster parameters because of a number of degeneracies affecting the data, so that we discarded those results.

We checked whether we could identify  $I$ -band excesses, but exclusion of the  $I$ -band filter did not produce any improvement of the fit in the  $\chi^2$  sense (as expected if the fit including the  $I$ -band photometry is correct). In this paper, we will thus only discuss the NGC 5253 cluster fit results based on application of our approach to (i) the full wavelength range and (ii) the range excluding the NIR filters.

#### 3.3 GALEV models and AnalySED approach

*Model-specific details.* Our second, complementary approach uses the GALEV SSP models (Kotulla et al. 2009; and references therein, as well as subsequent unpublished updates). They cover ages between  $4 \times 10^6$  and  $12.6 \times 10^9$  yr, with an age resolution of  $\Delta \log(t \text{ yr}^{-1}) = 0.05$ , and are based on

the latest set of stellar isochrones of the Padova group for metallicities of  $0.0001 \leq Z \leq 0.03$ , tabulated as 15 discrete metallicities. Our model grid was completed by inclusion of extinction effects (Calzetti et al. 2000), with  $E(B - V)$  spanning the range from 0.0 to 2.0 mag, and adopting a resolution of 0.05 mag.

*Parameter determination.* In recent years, we developed a sophisticated tool for star cluster analysis based on broadband SEDs, ANALYSED, which we tested extensively both internally (de Grijs et al. 2003a,b; Anders et al. 2004) and externally (de Grijs et al. 2005), using both theoretical and observed star cluster SEDs.

Note that in this paper we base our main analysis on the Yggdrasil models and analysis approach discussed in Section 3.2. We apply the ANALYSED approach to the exact same filter set as used in the IR-excess approach. This ensures that the results from both approaches are directly comparable.

For a given cluster, the shape of the observed SED (again, expressed in magnitudes), including the relevant observational uncertainties, was compared with the shapes of model SEDs (as a function of age, metallicity and foreground extinction) for the passband combination considered. Each model SED (and its associated physical parameters) was assigned a probability based on the  $\chi^2$  value of this comparison. The model data set with the highest probability (i.e., the lowest  $\chi^2$  value) was adopted as the most representative set of cluster parameters. Models with decreasing probabilities were summed up until a 68.26 per cent total probability ( $1\sigma$  confidence interval) was reached, to estimate the uncertainties in the best-fitting model (cf. Anders et al. 2004).

## 4 COMPARISON OF PARAMETER DETERMINATIONS

In the remainder of this paper, we will use our Yggdrasil models and associated analysis, and the resulting fundamental cluster parameters, as the basis for the ensuing discussion. In this section, we explain in detail how we determined which clusters are affected by an IR excess and pursue an approach in which we determine the basic cluster parameters. In Sections 4.1 and 4.2, we use the Yggdrasil models and analysis as our basis; in Section 4.3, we compare these results with those from application of the GALEV models and the AnalySED approach.

### 4.1 Determination of IR excesses

Based on application of our least-squares fitting routine to the full wavelength coverage available (i.e., all 10 filters with central wavelengths from 330 nm to 2.22  $\mu\text{m}$ ), we obtained best fits with sufficiently small  $\chi^2_\nu$  and  $Q > 0.001$  for 149 of the 182 objects in our sample with photometric uncertainties  $< 0.3$  mag in at least 7 filters. In the remainder of this paper, we will base our analysis on this reduced data set of 149 clusters and discard the 33 objects for which we could not achieve a satisfactory fit (we will briefly return to these objects below). A number of clusters returned best fits with  $\chi^2_\nu \gg 1$  and  $Q < 10^{-5}$ . We inspected the residuals, i.e., the differences between the observed SED and the model fit, in each of the  $N$  filters used for the fit (for all clusters, independent of the goodness-of-fit parameters) and confirmed that

30 objects were characterized by an IR excess with respect to the best-fitting model that included all NUV and optical filters up to and including F814W. The remaining 119 objects exhibited SEDs which could be fitted with ‘standard’ SSP models over the full wavelength range.

Fig. 5 shows comparisons of the resulting cluster parameters. On the horizontal axes, we plot the ages, extinction values and masses based on fits to the full F330W→F222M data set (10 filters), adopting a metallicity of  $Z = 0.004$  henceforth. On the vertical axes, we plot the results for the F330W→F814W 7-filter set. The 30 clusters with appreciable IR excess are shown as the objects contained in the (red) circles. Overall, there is a reasonable one-to-one correlation between the results from the two different data sets. As we already pointed out in de Grijs et al. (2005), the mass determinations are clearly better constrained than the age or extinction determinations. The latter are very sensitive to small changes (including those due to photometric problems) in the SEDs.

### 4.2 Systematic effects for all versus IR-excess sources

Both the age and the mass comparisons for the sources *exhibiting an IR excess* show that exclusion of the NIR points results in smaller values. For the mass determinations, this is expected at least to some extent, because masses are determined based on a scaling of the entire SED; excess intensity in a number of filters will hence artificially increase the scaling upwards. In addition, redder SEDs will result in older ages, and hence the resulting mass estimates will be based on incorrect mass-to-light ratios, because the latter are age-dependent. For the age determinations, the sources affected by an IR excess are artificially given older ages (and older clusters are assigned higher masses for the same luminosities), assuming fully sampled cluster mass functions.

For the full sample of 149 objects, we found that the exclusion of the NIR filters in our Yggdrasil-based analysis resulted in 112 objects that exhibited an age difference of  $\Delta \log t[\text{yr}] \leq 0.05$  dex. Eight objects were characterized by age differences of  $0.05 < \Delta \log t[\text{yr}] \leq 0.30$  dex, 18 objects resulted in  $0.30 < \Delta \log t[\text{yr}] \leq 0.50$  dex and for seven objects  $\Delta \log t[\text{yr}] \geq 1.0$  dex. The equivalent numbers for the differences in mass are 92 objects with  $\Delta \log M_{\text{cl}}[M_\odot] \leq 0.05$  dex, 27 exhibiting  $0.05 < \Delta \log M_{\text{cl}}[M_\odot] \leq 0.30$  dex, 16 for which  $0.30 < \Delta \log M_{\text{cl}}[M_\odot] \leq 0.50$  dex and only three showing a logarithmic age difference in excess of 1.0 dex.

We also checked whether our choice of metallicity may have affected the results through the well-known age–metallicity degeneracy. We refitted our entire data set, again using the two different filter combinations, but now adopting  $Z = 0.008$  for all clusters. The ages resulting from the  $Z = 0.008$  assumption were very similar to but marginally younger than those based on  $Z = 0.004$  (not shown). This effect translated in a small to negligible offset that did not appear to be a function of age. Thus, we conclude that our results are negligibly affected by the age–metallicity degeneracy (but see Section 4.3), and that adoption of a single metallicity for all clusters does not appreciably affect our analysis.

In Fig. 6 we compare the residuals of the fits obtained from single-mindedly fitting the entire available wavelength

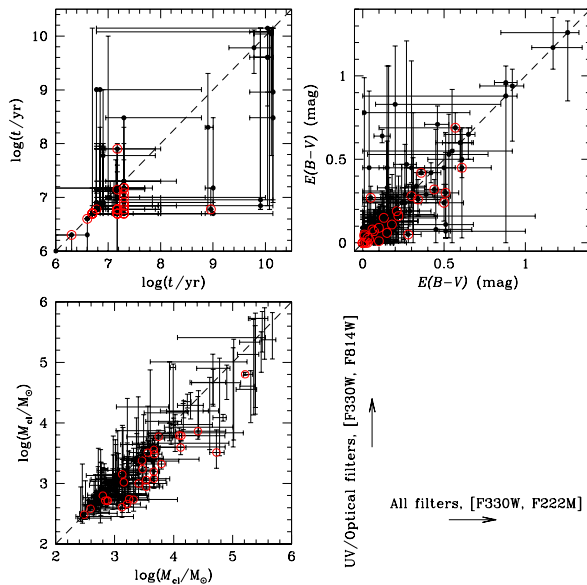


**Figure 5.** Comparison, using the models discussed in Section 3.2, of the fundamental cluster parameters as a function of wavelength coverage.  $X$  axis: all 10 filters;  $y$  axis: all 7 NUV and optical filters, up to and including F814W. The objects identified with (red) circles are characterized by an IR excess (see text for discussion). Note that our standard SED analysis returns similarly young ages for many of the cluster candidates (cf. Fig. 7, top left-hand panel). Therefore, the density of data points in the top left-hand panel appears lower than it is in reality.

range (shaded histograms) and those resulting after exclusion of the NIR passbands (open histograms drawn using solid lines), again for the clusters affected by an IR excess only. It is clear that the residuals in the latter case are more symmetrically distributed around zero. Note that the most significant effect is seen in the residuals of the F814W filter. These residuals improve upon exclusion of the NIR data because this allows us to obtain a ‘proper’ match (in the  $\chi^2$  sense) of all data points in the optical regime. Because of the flux excess in the NIR filters, in the fits including all 10 filters the observed F814W flux was consistently below the best model prediction.

Fig. 7 is a collection of the distributions of the basic cluster parameters for the full data set of 149 clusters. We show both the distributions initially obtained by fitting the entire available wavelength range (dotted histograms) and those resulting from NUV to optical filters only (solid lines). As in Fig. 5, we see that this filter selection leads to younger ages and lower masses, while the overall distribution of extinction values remains statistically unchanged. Note that the large majority of our sample clusters, particularly those exhibiting an IR excess (see also Fig. 5), have masses between a few  $\times 10^2$  and  $10^5 M_\odot$  (for confirmation of this mass range, see e.g., Harris et al. 2004; Cresci et al. 2005). These are most likely significantly affected by stochastic sampling of their stellar mass functions. Table 2 includes our final set of derived cluster parameters based on the Yggdrasil SSP models and associated analysis (assuming fully sampled mass functions).

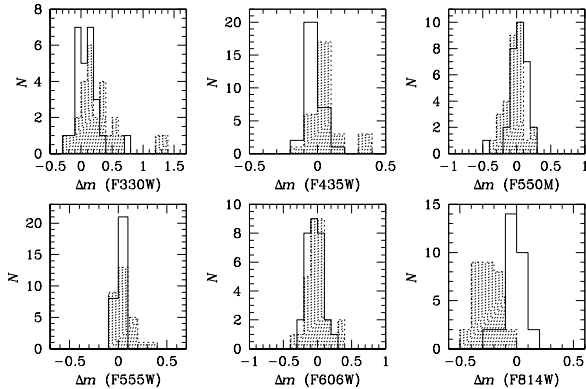


**Figure 6.** Fit residuals as a function of filter for the clusters affected by a significant IR excess. The shaded histograms are the residuals based on fits to the full available wavelength range; the solid histograms show the results after exclusion of the filters affected by the IR excess.

We also explored whether our results are affected significantly by the age–extinction degeneracy, which often causes artificial offsets if one has access to only broad-band SEDs covering smaller wavelength ranges. The optical–NIR colour–colour diagram of Fig. 8 clearly shows that the clusters in which we detected an IR excess are all located redward of the model SSP (blue solid line). This, therefore, serves as an independent check of the reality of our IR-excess determinations (see also fig. 2 of Cresci et al. 2005).

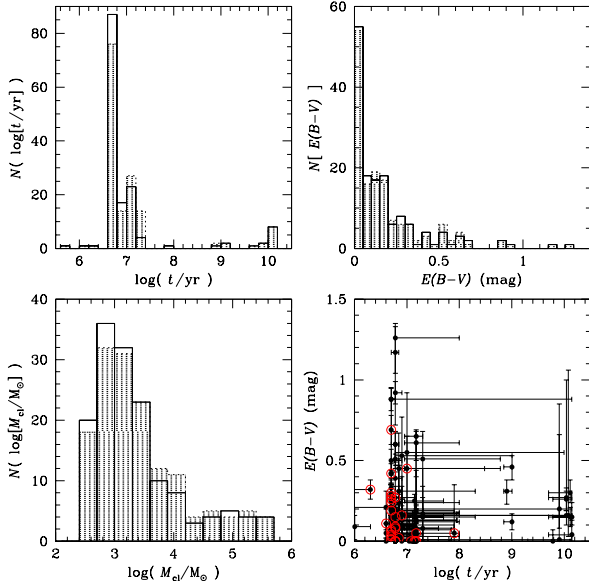
The large majority of IR-excess sources are located towards blue optical colours. If they were affected by significant extinction, we would have expected them to be displaced well along the direction of the reddening vector. However, since we have access to up to 10 data points spanning the entire NUV/optical/NIR range, this helps our efforts to break the age–extinction degeneracy quite significantly: for instance, the evolution in age and the extinction vector are not oriented parallel to each other in the colour–colour diagram of Fig. 8, at least for young ages (they would be in optical-only colour–colour diagrams). We thus conclude that the young IR-excess sources are, by and large, negligibly affected by the age–extinction degeneracy and, more importantly, that the IR excess in these sources is most likely not owing to the effects of extinction. For reference, we also included the 33 objects for which we could not obtain satisfactory fits using fully sampled SSP models in Fig. 8 (small blue crosses). Their distribution in colour–colour space follows that of the remaining 149 objects which are the main focus of this paper; a fraction also appears to exhibit an IR excess with respect to the standard SSP models.

### 4.3 One-to-one comparisons: dependence on the SSP model suite adopted

Finally, we compare the resulting masses and ages from our Yggdrasil models and analysis with those obtained based on the GALEV+ANALYSED approach: see Fig. 9 and Table 3. The top row of Fig. 9 shows the one-to-one comparisons of the clusters’ ages and masses (the resulting extinction values cannot be determined as reliably). While the overall trends show reasonable agreement, particularly for the masses (cf.

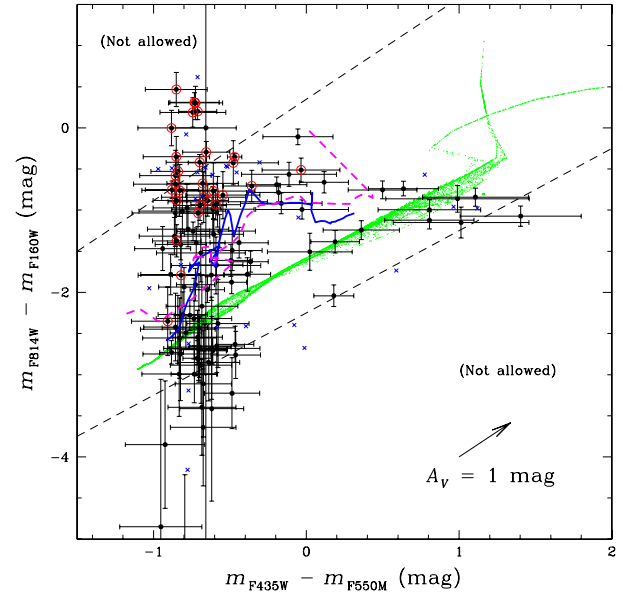
**Table 2.** NGC 5253 cluster coordinates and derived parameters assuming fully sampled Yggdrasil SSP models.<sup>a</sup>

ID	R.A. (J2000) (deg)	Dec. (J2000) (deg)	$\sigma_{G,F550M}$ (pixels)	$N_{\text{filters}}^b$	$\log(t)$ [yr]	Uncertainties		$\log(M_{cl})$ [ $M_{\odot}$ ]	Uncertainties	
						(positive)	(negative)		(positive)	(negative)
0	204.9766060	-31.6426963	1.154	...	...	...	...	...	...	...
1	204.9775826	-31.6427056	1.165	10	7.18	0.67	0.40	3.13	0.26	0.61
2	204.9810049	-31.6366573	1.194	10	7.15	0.03	0.37	3.04	0.13	0.46
3	204.9810436	-31.6368153	1.158	10	9.79	0.33	0.48	4.67	0.21	0.39
4	204.9792423	-31.6411761	1.154	10	6.78	0.03	0.03	2.71	0.10	0.03
...	...	...	...	...	...	...	...	...	...	...

<sup>a</sup> The full data table is available associated with the online version of this article. This stub is meant to provide guidance regarding form and content of the full table. <sup>b</sup> Number of filters used to obtain the derived parameters.**Figure 7.** Distributions of the fundamental NGC 5253 cluster parameters. The dotted histograms with dashed shading represent the parameters based on fits to the full wavelength range from the F330W to the F222M filter; the histograms drawn using solid lines are the resulting distributions after removal of the NIR filters from the SED analysis. The bottom right-hand panel shows the distribution of our sample clusters in the age–extinction plane (see Section 6.4). The objects identified with red circles are characterized by an IR excess.

de Grijs et al. 2005) as well as for most of the IR-excess sources, there are a few discrepancies (indicated by the dotted circles) that require further investigation.

Fig. 10 displays the SEDs of the four clusters for which our Yggdrasil-based analysis and the ANALYSED approach obtained the most different age estimates [ $\Delta t$  (yr)  $> 2\sigma$ ]. The latter returned an age for cluster 107 (indicated by the small dotted circle in the top left-hand panel of Fig. 9) of  $2.0 \pm 0.8$  Gyr and an extinction value of  $E(B-V) = 0.0$  mag, while our Yggdrasil-based analysis resulted in estimated age and extinction values of  $6.0 \pm 0.7$  Myr and 0.60 mag, respectively, for similar-quality fits. Clusters 100, 130 and 167 (contained in the large dotted circle in the same panel) are also clearly discrepant because of the age–extinction degeneracy: the (age, extinction) pairs for each of these clusters are, respectively, (4.5 Myr, 1.05 mag) versus (11.2 Gyr, 0.25 mag),

**Figure 8.** Colour–colour diagram in the ST mag system. Blue heavy solid versus magenta heavy dashed line: GALEV versus Yggdrasil SSP models for  $Z = 0.004$ , spanning an age range from 3 Myr (blue extremities) to  $\sim 12$  Gyr (red extremities of the models). Green points: Theoretical stellar loci (Marigo et al. 2008); small blue crosses: Objects for which we could not obtain a satisfactory fit using fully sampled SSP models. The objects identified with red circles are characterized by an IR excess. The black dashed line delineates the region in colour–colour space where star clusters and individual stars may be found (taking into account realistic photometric uncertainties).

(5.0 Myr, 1.10 mag) versus (11.2 Gyr, 0.25 mag), and (4.5 Myr, 0.90 mag) versus (12.6 Gyr, 0.05 mag), where the first and second (age, extinction) pairs refer to the results from the ANALYSED and Yggdrasil-based analyses, respectively. Additionally, differences between both sets of models and the details of the fitting routines may contribute to a lesser extent. The significantly different age estimates for these four clusters are associated with similarly varying mass-to-light ratios, which in turn also lead to significant differences in the resulting mass estimates. This effect is seen in the top right-hand panel of Fig. 9, where the objects of relevance are indicated by the large dotted circle.

Despite these differences for a small number of clusters, the main features in the overall age and mass distributions

**Table 3.** NGC 5253 cluster parameters derived assuming fully sampled GALEV SSP models.<sup>a</sup>

ID	log( <i>t</i> ) [yr]	Uncertainties		log( <i>M</i> <sub>cl</sub> ) [ <i>M</i> <sub>⊙</sub> ]	Uncertainties	
		(positive)	(negative)		(positive)	(negative)
0	...	...	...	...	...	...
1	6.65	0.05	0.05	2.62	0.11	0.03
2	6.65	0.55	0.05	3.24	0.18	0.32
3	6.60	0.15	0.05	2.70	0.32	0.03
4	7.00	0.35	0.05	3.73	0.48	0.10
...	...	...	...	...	...	...

<sup>a</sup> The full data table is available associated with the online version of this article. This stub is meant to provide guidance regarding form and content of the full table.

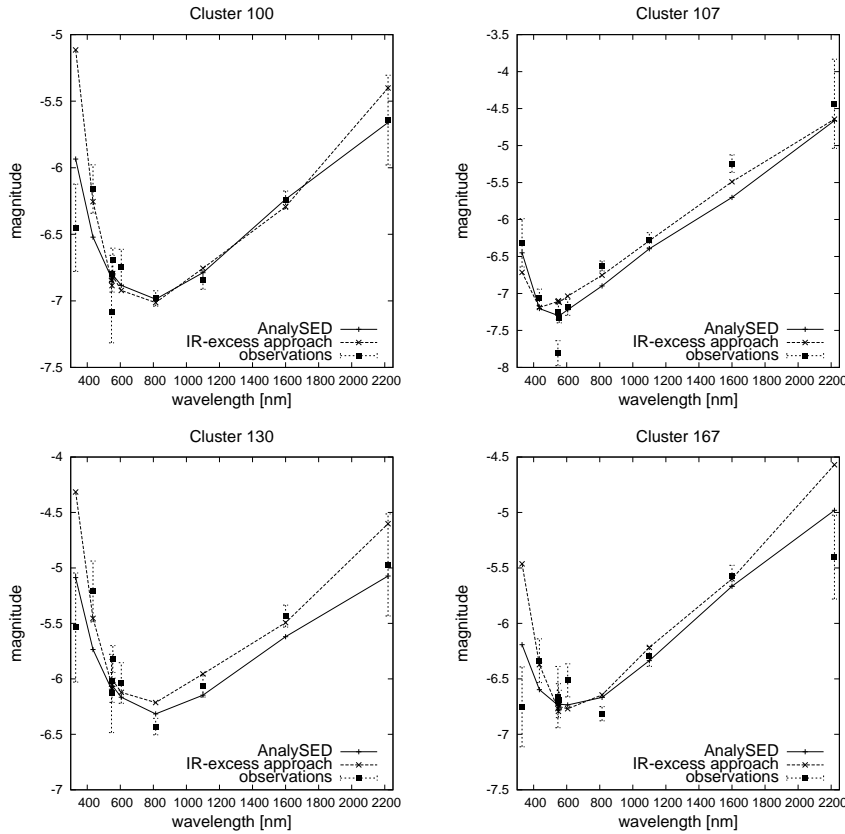


**Figure 10.** SEDs (absolute magnitudes in the ST mag system) of clusters 100, 107, 130 and 167 (contained in the dotted circles in Fig. 9), showing the effects of the age–extinction degeneracy (see text). The model SEDs are all based on GALEV models, adopting the best-fitting ages and extinction values derived from the ANALYSED and Yggdrasil-based (‘IR-excess’) approaches.

(bottom row) are fairly well reproduced by both independent approaches. Assuming a simple underlying skewed Gaussian distribution, the peak in the age distribution resulting from our ANALYSED analysis (including all objects) occurs at  $\langle \log(t \text{ yr}^{-1}) \rangle = 7.11$ , with  $\sigma_{\langle \log t \rangle} = 0.80$ . For comparison, the Yggdrasil-based analysis returned  $\langle \log(t \text{ yr}^{-1}) \rangle = 7.10$ , with  $\sigma_{\langle \log t \rangle} = 0.94$ . For the mass distributions, we find  $\langle \log(M_{\text{cl}}/M_{\odot}) \rangle = 3.38$  versus 3.37, and  $\sigma_{\langle \log M_{\text{cl}} \rangle} = 0.76$  versus 0.77, respectively. This excellent correspondence is much better than the feature-reproduction robustness reported in de Grijs et al. (2005), where we quoted reproducibilities of  $\Delta \langle \log(t \text{ yr}^{-1}) \rangle \leq 0.35$  and  $\Delta \langle \log(M_{\text{cl}}/M_{\odot}) \rangle \leq 0.14$ .

If we compare the age and mass determinations for

the individual clusters, a similar result emerges. The mean differences between the Yggdrasil-based analysis and the ANALYSED results is  $\langle \Delta \log(t \text{ yr}^{-1}) \rangle = 0.041$  and  $\langle \Delta \log(M_{\text{cl}}/M_{\odot}) \rangle = 0.100$ , respectively, with spreads (Gaussian  $\sigma$ 's) of 0.900 and 0.517 dex, respectively.

#### 4.4 To which extent does H $\alpha$ photometry make a difference?

So far, we have focussed on the power of (medium- and) broad-band SED analysis based on extensive wavelength coverage. This is the type of observational data one might expect to obtain most easily for any extragalactic star clus-

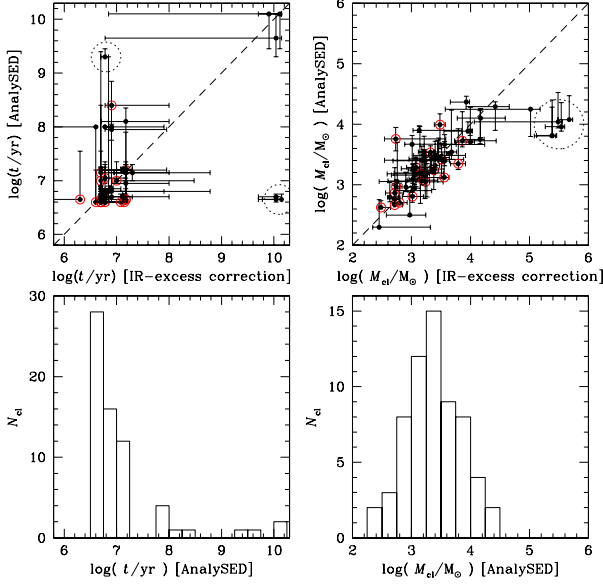


**Figure 9.** (*top*) Comparison of the individual cluster ages and masses based on application of our two different SSP-matching approaches. The objects identified with (red) circles are characterized by an IR excess. The dotted circles indicate the handful of sources which are most likely significantly affected by the age–extinction degeneracy (see Section 4.3). (*bottom*) Age and mass distributions based on application of the ANALYSED approach.

ter system, and hence exploration of the limitations of such a data set is relevant. For our analysis of the specific star cluster sample of NGC 5253, we also obtained narrow-band F658N observations from the *HST* Data Archive, covering the  $H\alpha$  emission line.<sup>6</sup> For most of the NGC 5253 clusters, numerous authors, including Calzetti et al. (1997) and Cresci et al. (2005), provide support for the young ages resulting from their fits by referring to the  $H\alpha$  fluxes found associated with these objects.  $H\alpha$  fluxes have also been found useful for analyses of numerous other YSC systems (for recent references, see e.g., Chandar et al. 2011; Whitmore et al. 2011; Fousneau et al. 2012; and references therein), although the present analysis represents the first full integration of  $H\alpha$  photometry in a simultaneous multi-passband ( $N > 4$  filters) approach.

In this section, we add the F658N/ $H\alpha$  photometry to our SEDs for confirmation and reanalysis of the properties of the NGC 5253 clusters using the Yggdrasil models. We obtained two sets of F658N photometry for our star cluster sample. First, we adopted the same apertures as for the nearest continuum filter, F550M. However,  $H\alpha$  emission may be more extended than that of the associated continuum sources. As such, we determined the Gaussian  $\sigma_G$ 's on the F658N image itself and used these size estimates to determine a second set of F658N magnitudes (using the source,

<sup>6</sup> Note that NGC 5253 was also observed through a narrow-band filter covering the  $H\beta$  line. Calzetti et al. (1997) already extensively explored the galaxy's morphology and dust properties based on these observations, so that we will not repeat that analysis here.

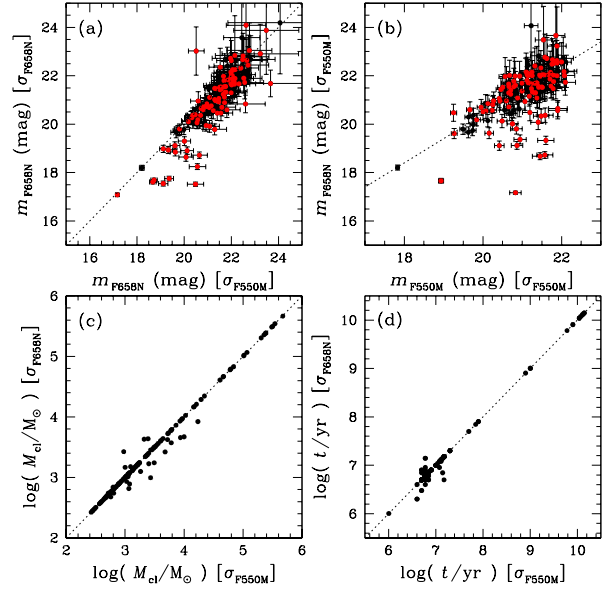


**Figure 11.** (a) F658N photometry as a function of aperture size based on the intrinsic Gaussian  $\sigma_G$ 's in the F550M and F658N images using the individualized apertures defined in Section 2.3. Red data points: objects younger than 10 Myr; dotted line: locus of equality. (b) Cluster photometry in the F550M and F658N filters, using aperture sizes based on  $\sigma_{G,F550M}$ . Dotted line: locus of equality corrected for the difference in filter transmission windows. (c) and (d) Mass and age comparisons, respectively, obtained using the photometry based on the differently sized apertures from panel (a). We have left out the relevant error bars for presentational clarity. All panels include the data or derived properties for all 149 clusters in our final sample.

inner and outer sky radii expressed in units of  $\sigma_G$  as defined in Section 2.3). A comparison of Gaussian sizes (not shown) indicates that the  $H\alpha$  emission coincident with our sample clusters exhibits a much broader range than the associated continuum emission in the F550M filter.

Fig. 11a shows the resulting F658N photometry as a function of aperture size used. Although a reasonable one-to-one correlation between the F658N magnitudes resulting from using aperture sizes based on the F550M and F658N  $\sigma_G$ 's is apparent, there is a clear offset to brighter magnitudes if the F658N-based size criterion is used, particularly for objects returned as younger than 10 Myr, based on the Yggdrasil-based broad-band analysis (indicated in red). This underscores the need to account for differences in source sizes as a function of passband.

Panel (b) shows the distribution of our sample clusters in the F550M versus F658N magnitude plane (the latter includes both continuum and line flux, if present). Again, the red data points are the objects younger than 10 Myr and the dotted line is the locus of equality, corrected for the difference in filter transmission windows. This panel shows that all sources that are more than twice their photometric  $1\sigma$  uncertainties from the dotted line are young ( $< 10$  Myr). Note that we used the same apertures here for both axes, so that we can properly compare the presence of any  $H\alpha$  excess.

Figs 11c and d compare the masses and ages, respec-

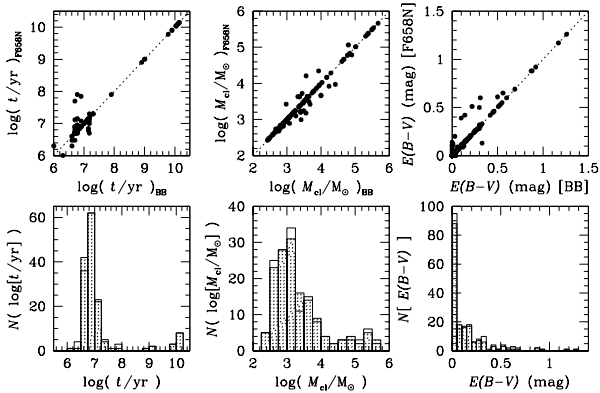


**Figure 12.** (top row) One-to-one comparisons for the full sample of 149 clusters of the ages, masses and extinction values based on using our medium- and broad-band photometry only (‘BB’), and that based on also including the F658N data. (bottom row) Dotted histograms: distributions based on the medium- and broad-band data only; solid histograms: based on additional inclusion of the F658N fluxes.

tively, obtained using the photometry based on the differently sized apertures shown in panel (a). We have left out the error bars for presentational clarity (see, e.g., Fig. 5 for guidance). These panels show that the impact of the different aperture sizes is very small, even at ages where significant  $H\alpha$  emission may be expected.

In Fig. 12 (top row) we compare the ages, masses and extinction values based on using our (medium- and) broad-band photometry only (‘BB’), and that based on including the F658N data. The bottom row shows the equivalent histograms of these parameters. The dotted histograms are the distributions based on the (medium- and) broad-band data only; the solid histograms are based on additional inclusion of the F658N fluxes. The differences, in any of the panels, are very small and statistically negligible. This is exemplified by a quantitative comparison of the histograms’ characteristics. The peak and Gaussian width of the age distribution resulting from our analysis including the F658N photometry are  $\langle \log(t \text{ yr}^{-1}) \rangle = 7.13$  and  $\sigma_{(\log t)} = 0.94$  dex, respectively, compared with 7.10 and 0.94 dex for the analysis based on the (medium- and) broad-band images only. Similarly, the mean and Gaussian width of the equivalent mass distributions are  $\langle \log(M_{\text{cl}}/M_{\odot}) \rangle = 3.36$  and  $\sigma_{(\log M_{\text{cl}})} = 0.77$  dex, respectively, versus 3.37 and 0.76 dex. We thus conclude that the  $H\alpha$  photometry fully supports our age and mass determinations of the NGC 5253 cluster sample based on medium- and broad-band photometry alone.

## 5 INITIAL ASSESSMENT OF THE EFFECTS OF STOCHASTICITY

Stochastic sampling of the stellar mass function, particularly of the massive stars in relatively low-mass ( $\lesssim$  a few  $\times 10^4 M_{\odot}$ ) – and therefore relatively poorly populated – clusters, may significantly affect the determination of fundamental cluster parameters based on broad-band SEDs (e.g., Cerviño, Luridiana & Castander 2000; Cerviño et al. 2002; Cerviño & Luridiana 2004, 2006; Barker et al. 2008;

Maíz Apellániz 2009; Popescu & Hanson 2010; Fouesneau & Lançon 2010; Fouesneau et al. 2012; Popescu, Hanson & Elmegreen 2012). In general, stochastic sampling of cluster stellar mass functions leads to broad, asymmetric colour distributions compared with the equivalent distributions associated with fully sampled SSP models and, as a consequence, important local biases are introduced in cluster age determinations for masses  $M_{\text{cl}} \lesssim$  a few  $\times 10^4 M_{\odot}$ . The resulting cluster masses are usually less affected by stochastic sampling than the corresponding age estimates; they tend to scatter around the equivalent mass determinations derived using the traditional approach.

Inspection of the derived cluster masses in Figs 7 and 9 clearly indicates that the majority of our sample clusters may be affected by stochastic sampling of their mass functions (cf. the mass ranges quoted in Harris et al. 2004; Cresci et al. 2005). This observation is further compounded by the results of our age determinations (based on the assumption of fully sampled SSPs!), which imply that a large fraction of the NGC 5253 clusters have ages near  $10^7$  yr (as confirmed and tightly constrained by the  $H\alpha$  analysis in Section 4.4).

This corresponds to stellar population ages when luminous red stars are present. Red-supergiant stars (RSGs; with stellar masses up to  $\sim 40 M_{\odot}$ ), in particular, start to appear around this time in realistic stellar populations, while at the same time the massive, hot, ionizing stars that dominate at young ages may cause significant variations in the nebular emission from stochastically sampled clusters (e.g., Cerviño et al. 2000; Fouesneau et al. 2012). These stars are significantly brighter than their main-sequence counterparts, but not proportionally more massive. The absence or presence of a small number of such stars can significantly affect the observed integrated colours of a cluster. For instance, stochastic effects are expected to affect the colour and magnitude of a 10 Myr-old,  $10^5 M_{\odot}$  cluster by  $\Delta V = 0.08$  and  $\Delta(V - I) = 0.07$  mag (Dolphin & Kennicutt 2002). In addition, these sources are relatively short-lived, and so the luminosity of the clusters might be expected to vary significantly on short timescales (e.g., Kiss et al. 2006; Szczygiel et al. 2010; and references therein). This is of particular interest and relevance in the present context because our observational data were taken over a period spanning a total of  $\sim 11$  years between the first and final images included in this study (proposal IDs 5479 and 10609, respectively).

We can obtain a better (initial) handle on the significance of the stochastic sampling effects associated with our cluster sample by examining Fig. 8 in detail. First, we note that most of our clusters are young and relatively unaffected by extinction. For  $A_V = 0$  mag, it appears that most of the clusters can be explained by a young age ( $\lesssim 10^8$  yr). However, in this case neither clusters redder than  $(m_{F435W} - m_{F550M}) = 0.4$  mag, nor those redder than the  $(m_{F814W} - m_{F160W})$  values defined by the SSP models can be explained. This implies that at least some amount of extinction is required to match the distribution of the clusters in colour–colour space. In addition, clusters that are redder in  $(m_{F814W} - m_{F160W})$  than the envelope of the SSP models with variable extinction are most likely explained by the presence of individual stars. This includes the majority of objects we identified as having an IR excess. (Note that we cannot exclude the possibility that, in a small number of cases, an additional photon source that is unaccounted

for may also give rise to their violation of the observational boundaries for genuine stars and SSPs.)

As such, we conclude that the IR excesses observed in 30 of the NGC 5253 clusters are consistent with the effects of stochastic sampling. Similarly, the additional clusters found in the same part of the colour–colour diagram are likely also affected by stochastic sampling if we adopt the same reasoning. This includes 30–40 per cent of the total sample discussed in this paper.

A first investigation focussing on the accuracy of derived cluster ages obtained along similar lines as done in this paper was published by Silva-Villa & Larsen (2011). We are in the process of implementing direct stochastic modelling using the GALEV SSPs as our basis. A preliminary comparison of our models with the results of Silva-Villa & Larsen (2011) indicates good agreement (E. Silva-Villa, priv. commun.). We note, however, that we are introducing important improvements with respect to their work. In particular, our observations of the NGC 5253 cluster system cover a much larger wavelength range, while we are also investigating the effects of extinction as a free parameter in our fits. A much more in-depth investigation of the effects of stochastic sampling on the ages and masses determined based on broad-band photometry will be published in Paper II. Once we have fully validated our stochastic modelling approach, we will undertake a detailed study of the effects of stochastic sampling on the derivation of the NGC 5253 fundamental cluster parameters (Paper III). This will have important consequences for our understanding of the system, given that many clusters have masses in the regime that is dominated by stochastic sampling effects. The current cluster parameters will then provide a very useful comparison data set.

## 6 PHYSICAL STATE OF THE NGC 5253 CLUSTER POPULATION

### 6.1 The cluster age distribution

Fig. 13 shows the distribution of our final, well-fitted NGC 5253 star cluster sample (of 149 objects) in the diagnostic age–mass plane, as well as the age and mass distributions resulting from our IR-excess analysis. The cluster population is dominated by a significant number of relatively low-mass ( $M_{cl} \ll 10^5 M_{\odot}$ ) objects. Assuming fully sampled stellar mass functions, these objects have ages from a few  $\times 10^6$  to a few  $\times 10^7$  yr. This age range is in excellent agreement with the starburst age of the host galaxy,  $\leq 10$  Myr, and is confirmed by our age redeterminations based on the clusters’ H $\alpha$  fluxes.

Our analysis has also revealed the presence of a small number of intermediate-age ( $\sim 1$  Gyr-old),  $\sim 10^5 M_{\odot}$  clusters, as well as up to a dozen old clusters resembling true globular clusters (GCs), in relation to both their ages ( $\sim 10$  Gyr) and masses ( $\gtrsim 10^5 M_{\odot}$ ). We emphasize that our discovery of a small number of old GCs is secure. First, in our analysis we use a low metallicity of  $Z = 0.004$  ( $0.2Z_{\odot}$ ). It is expected that the oldest stellar population components in a given galaxy are characterized by the lowest metallicity, since they were formed at a time when there was little recycled gas in the interstellar medium. (This argument is valid under the assumption that these clusters formed in NGC

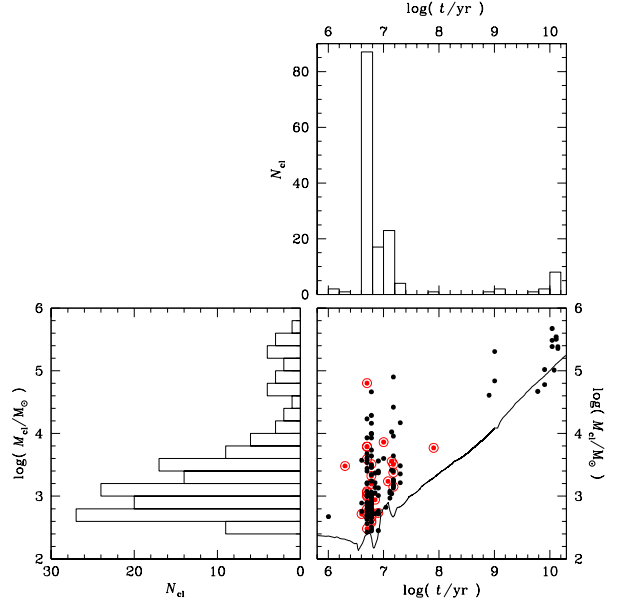


**Figure 13.** Age–mass distribution of the NGC 5253 clusters. The objects identified with (red) circles are characterized by an IR excess. The solid line in the age–mass plane represents our average, galaxy-wide detection limit at  $M_V \simeq -5.4$  mag ( $V \simeq 22.1$  mag), based on the SSP models adopted. For reasons of presentational clarity, we do not include error bars on the individual data points.

5253 and were not subsequently accreted; see below.) Our age estimates at the current low metallicity are already almost as old as the oldest ages in our SSP models, whereas at such old ages SSP models are quite insensitive to changes caused by metallicity differences. We confirmed that adopting an even lower metallicity will not result in a different conclusion.

In Fig. 13, we have also indicated the expected detection (50 per cent completeness) limit based on standard SSP analysis (solid line); the limit is a steeply increasing function of cluster mass with increasing age. Although we did not set out to select a statistically complete sample of star clusters, it is satisfying to note that our sample clusters obey a similar, galaxy-wide average detection limit across the entire age range. We focus specifically on resolved yet compact clusters (for which it is straightforward to obtain the integrated photometry and a generic completeness limit) rather than on more dispersed stellar associations (cf. Annibali et al. 2011). This also enables a better comparison with previous studies of this galaxy, many of which were based on lower-resolution images than used in the present study.

The selection of the final sample shown in Fig. 13 is governed by our observations with the lowest S/N. Depending on the nature of the clusters (i.e., with or without an IR excess), the images with the lowest S/N are the F330W and the F222M observations, respectively. The complex behaviour of the selection limit resulting from the data reduction and analysis steps, combined with the galaxy’s highly variable background, renders determination of the ‘true’ detection limit less than trivial. In addition, the effects of stochasticity will also play a role in the (non-)detection of the clusters closest to the detection limit (e.g., Silva-Villa & Larsen

2010, 2011). Keeping in mind both of these issues, so that it is unrealistic to assign a single detection limit to the entire galaxy, the distribution of the data points in Fig. 13 implies that the *average*, galaxy-wide detection limit is  $M_V \simeq -5.4$  mag ( $V \simeq 22.1$  mag), but we note that local variations, combined with the effects of stochasticity, could be up to 0.3 mag.

Given the number and concentration of old GCs above our detection limit in the NGC 5253 data, we speculate that these are merely the surviving high-mass, high-luminosity clusters of an initially much larger population of clusters that formed around the time of galaxy formation, many of which may have been disrupted or naturally faded to below the detection limit because of stellar evolution. The young clusters are distributed in two narrow ‘chimneys’ near  $\log(t \text{ yr}^{-1}) = 6.7$  and  $7.2$ , which are caused by the features in SSP models around that age (cf. the ‘wiggles’ in the SSP model used to indicate the selection limit in Fig. 13), but are not necessarily associated with stochastic sampling of their mass functions. In reality, we would expect these clusters to be spread out more evenly across this young age range.

The clusters in both chimneys are distributed randomly throughout the galaxy, similarly for objects with both  $\log(t \text{ yr}^{-1}) \leq 7.0$  and  $7.0 < \log(t \text{ yr}^{-1}) \leq 8.0$ . The YSCs characterized by a clear IR excess are confined to the galaxy’s main body; the intermediate-age clusters in NGC 5253, with ages  $\log(t \text{ yr}^{-1}) \simeq 9$ , are found in the galaxy’s outer region (cf. Harbeck et al. 2012), towards the south.

Finally, the complement of  $\gtrsim 10$  Gyr-old clusters are predominantly located in the southeast of the main body of NGC 5253 (cf. Fig. 2). Since our observational data reach similar depths across the galaxy (except for the central region on the East featuring a wide dust lane), we would have expected to detect such old massive clusters across the galaxy with a similar level of confidence. As such, we conclude that this spatial bias is likely real.

If these clusters were moving on chaotic, freely tumbling orbits through the galaxy, one would have expected them to be well mixed on these long timescales. However, Kobulnicky & Skillman (1995) showed, based on observed HI gas dynamics, that the main body of the galaxy appears to be rotating as a solid body along the galaxy’s *major* axis. Under these circumstances, clusters that formed at one end of the gaseous central bar or disc, may have remained confined to a small area since the time of their formation. Alternatively, the old clusters could have been accreted externally: to explain the galaxy’s peculiar velocity field, Kobulnicky & Skillman (1995) also suggested that accretion of a low-metallicity, gas-rich companion galaxy on a highly inclined orbit is highly plausible (but see Davidge 2007). This interpretation is supported by the unusual weakness of the galaxy’s CO emission, the morphology of the CO gas and its unusual kinematic properties (Turner et al. 1997).

## 6.2 Red- and infrared-excess sources

We also note that almost all clusters affected by an (infra-)red excess, are found among the YSC population in clusters with masses  $\lesssim 10^4 M_\odot$ . Adamo et al. (2010a,b, 2011a,b) identified two possible reasons for the occurrence of an (infra-)red excess in more massive clusters in their sample BCG galaxies. For clusters younger than approxi-

mately 6 Myr, they suggested that the IR excess could be due to diffuse, hot dust in which these YSCs may still be embedded and/or a large fraction of young stellar objects and pre-main-sequence (PMS) stars. In the optical *I* band (F814W), the shallower red excess observed in such YSCs may be owing to a dust photoluminescence bump in their SEDs at  $0.7\text{--}0.9 \mu\text{m}$ , often seen in the presence of very strong UV fields. Older clusters, with ages  $\gtrsim 10$  Myr, may exhibit an IR excess, which these authors attribute to the uncertain treatment of RSG stars in SSP models or the effect of stochasticity in the stellar mass function. In NGC 5253, we have probed to much lower masses than Adamo et al. (2010a,b, 2011a,b) could reach in their more distant BCG sample.

Most of our IR-excess clusters are found in the younger ‘chimney’, characterized by an age of  $\sim 5 \times 10^6$  yr. This is close to the lower age limit of our SSP models and also close to the age when YSCs are expected to become optically visible (i.e., after dispersion of at least some of the embedded dust associated with their formation process), so that a number of these clusters may have even younger ages. Based on the detailed studies referenced above, these clusters are most likely affected by a combination of stochastic sampling effects and the presence of PMS stars. The IR-excess clusters in the older chimney, at  $\log(t \text{ yr}^{-1}) = 7.1\text{--}7.2$  are also of relatively low mass and, hence, we expect them to be affected by stochastic sampling effects, while at this age the stochastic colour variations owing to RSG stars will also become apparent.

Only two of our IR-excess clusters allow us to offer a less ambiguous explanation. The highest-mass cluster affected by an IR excess has a mass of almost  $10^5 M_\odot$ . Although it has been assigned an age of  $\sim 4 \times 10^6$  yr, stochastic sampling should only play a minor role, so that we are confident that the excess in this case is caused by the presence of a hot, diffuse dust cocoon or perhaps young stellar objects. The oldest cluster affected by an IR excess has an age of almost  $10^8$  yr. Although it has a low mass of  $\sim 6 \times 10^3 M_\odot$ , so that stochastic sampling effects must duly be taken into account, this is also the time when (relatively short-lived) AGB stars appear in realistic stellar populations, playing a similar role as RSG stars at ages near  $10^7$  yr, both in terms of the numbers present at a given time and their short lifetimes.

## 6.3 Comparison with previous studies based on fully sampled stellar mass functions

Cresci et al. (2005) published the most recent statistical study of the NGC 5253 cluster population (see also Harris et al. 2004). They based their results on *HST* F547M and F814W broad-band observations and ground-based  $K_s$ -band observations with the Very Large Telescope, complemented with *HST*-based  $H\alpha$  data. Qualitatively, our results are similar to theirs, although there are a number of important differences. They divide their final cluster sample of 115 sources into a ‘young’ subsample of 51 objects which were detected in the  $H\alpha$  filter, and an ‘old’ subsample.

For the ‘young’ subsample, they derive ages spanning the range from 3 to 19 Myr. This corresponds to the bulk of the clusters in our two young chimneys in Fig. 9. To derive the cluster masses, they assumed an average extinction of  $A_V = 0.98$  mag – which appears reasonable for most clusters

based on our extinction estimates in Fig. 7 and assuming a Calzetti et al. (2000) extinction law – and an average age of 8 Myr; for the ‘old’ clusters they assumed an average age of 20 Myr (cf. Harris et al. 2004). Above their 50 per cent completeness limit, they find a steeply declining number of clusters with increasing mass, with a maximum mass of  $\sim 10^6 M_{\odot}$ . Our mass function (Fig. 9) samples significantly lower-mass clusters.

Contrary to their analysis, however, we believe that we do not have sufficient numbers of clusters to comment on the reality (or otherwise) of a ‘peak’ in the mass function. Their result may be an artefact of the steeply increasing incompleteness limit with increasing age which could mask the true underlying mass distribution and produce an artificial turnover in the observed mass distribution (cf. Fig. 13).

Prior to their work, Calzetti et al. (1997) used optical *HST*/WFPC2 broad- and narrow-band observations in a careful attempt to characterize the star cluster properties in the core of NGC 5253. Tremonti et al. (2001) used *HST*/STIS UV spectroscopy of four of the brightest clusters in the galaxy’s central region to derive their fundamental properties. Of the four clusters examined in detail in both the Calzetti et al. (1997) and Tremonti et al. (2001) studies, we managed to produce satisfactory results for three using our broad-band-only SED fitting routines. Using Calzetti et al.’s (1997) nomenclature, these are clusters NGC 5253-1, 2 and 6 (corresponding to, respectively, objects 129, 45 and 36 in Table 2). For NGC 5253-1, Calzetti et al. (1997) derive an age of 8–12 Myr, while we find a best-fitting age of  $14 \pm 3$  Myr. Calzetti et al. (1997) and Tremonti et al. (2001) find ages of, respectively, 50–60 and  $8^{+2.6}_{-0.9}$  Myr for NGC 5253-2, compared with our best age estimate of  $5.0 \pm 1.6$  Myr. Our results thus support the younger age advocated by Tremonti et al. (2001), although our mass estimate,  $(6.4 \pm 1.3) \times 10^4 M_{\odot}$  is somewhat higher than theirs,  $\sim 1 \times 10^4 M_{\odot}$ . Note that although this cluster’s derived mass tends towards the mass range where the effects of stochastic sampling become smaller, we caution that a small number of luminous red stars could easily affect its broad-band SED to mimic a younger age. Finally, for NGC 5253-6, Calzetti et al. (1997) find a best-fitting age of 10–17 Myr, which is a close match to our age estimate,  $14 \pm 2$  Myr.

We also compared our derived age and mass estimates with the equivalent results of Harris et al. (2004). Within the uncertainties associated with both sets of parameter determinations, our age and mass determinations of the dozen objects with parameter determinations in common are fully consistent with theirs (not shown).

Recently, Harbeck et al. (2012) reported the discovery of three potentially massive clusters ( $M_{\text{cl}} \geq 10^5 M_{\odot}$ ) with ages of order 1–2 Gyr in the galaxy’s outer regions, based on *HST*/ACS imaging observations in the F415W, F555W and F814W filters. These clusters, which they refer to as #2, 6 and 7, form part of a more extensive population of intermediate-age and old clusters. From an initial focus on the galaxy’s starburst core and its properties, more recent studies have attempted to explore the galaxy’s overall star-formation history. The intermediate-age clusters of Harbeck et al. (2012), as well as our larger population of intermediate-age and old clusters support the notion that NGC 5253 is a very active dwarf starburst galaxy that has undergone multiple episodes of star and star cluster formation (see also

Calzetti et al. 1997 and McQuinn et al. 2010a,b for similar conclusions based on studies of the field-star population).

#### 6.4 The cluster size distribution in the context of previous work

Next, we consider the cluster size distribution shown in Fig. 1 in the context of previous work. Harbeck et al. (2012) tabulate the FWHMs of the 28 objects in the galaxy’s outer regions which they discuss (18 likely clusters and 10 background galaxies). Their resulting size distribution (converted to Gaussian  $\sigma$ ’s) is generally flat, however, and does not show a clear peak at smaller sizes similar to what we find in this paper. This is likely caused by their cluster selection procedure, which was based on visual inspection of the ACS images. In addition, we cannot directly compare our cluster parameters derived in this paper with Harbeck et al.’s (2012) results, because both samples are complementary, without any spatial overlap.

Harris et al. (2004) also examined the NGC 5253 cluster sizes and include a figure showing their (FWHM) size distribution as a function of cluster magnitude. Their size distribution is based on analysis of their F547M image (which is closest in wavelength to the F555W filter we used). The vast majority of their sample clusters have sizes which are similar to the PSF size, with a small tail towards more extended clusters. Although this trend is qualitatively similar to our result, we point out that their size measurements were based on WFPC2/WF camera images, which have a factor of approximately 2 lower resolution than the ACS/HRC images upon which we base our analysis. The bottom inset in Fig. 1 shows the equivalent figure for our data set, also using the F547M magnitudes. The trend shown is similar to that found by Harris et al. (2004). We re-emphasize here that we specifically selected objects that appeared compact, which implies that we selected against including stellar associations.

Finally, we consider the cluster size distribution in a wider context. Bastian et al. (2005) examined the effective radius ( $R_{\text{eff}}$ ) distribution of their YSC sample in M51 and of the old GCs in the Milky Way. They represented the distribution by a power law of the form  $N(R)dr \propto r^{-\eta}dr$ , and found best-fitting power-law indices of  $\eta = 2.2 \pm 0.2$  and  $2.4 \pm 0.5$  for the M51 and Milky Way clusters, respectively. This compares to  $\eta = 3.4$  for the YSCs in the merger remnant galaxy NGC 3256 (Ashman & Zepf 2001). Here, we find a best-fitting power-law distribution of the clusters’ Gaussian  $\sigma$ ’s characterized by  $\eta = 2.8 \pm 0.6$ , which agrees to within the uncertainties with these previous determinations – provided that there is a one-to-one correlation between  $R_{\text{eff}}$  and  $\sigma_{\text{G}}$ , which is a reasonable assumption if cluster profiles do not differ too significantly among galaxies.

## 7 SUMMARY AND CONCLUSIONS

Because of the wealth of available multi-wavelength data sets in the *HST* Data Archive, we chose NGC 5253 as target to compare two model approaches to determine fundamental star cluster parameters based on up-to-date input physics. We have gone significantly beyond previous studies of the NGC 5253 star cluster population.

First, although we still used medium-, broad-band and H $\alpha$  imaging observations, we base our results on the highest-achievable spatial resolution. The gain in resolution compared to previous studies is of order a factor of two in both dimensions, while our accessible wavelength range transcends previous studies by incorporation of both the NUV and NIR passbands. Crucially, this allows us to at least partially break the age–metallicity and age–extinction degeneracies. Second, we applied two spectral synthesis methods to our *HST* observations in up to 10 filters, taking into account the updated effects of nebular emission and the improved physical understanding of the excess flux at red optical and IR wavelengths found for a subset of young clusters.

We used the most recent models to explore the origin of excess emission of a fraction of the YSCs in optical *I* and longer-wavelength NIR filters compared to ‘standard’ SSP models, assuming fully sampled stellar mass functions. Of the 182 objects in our sample with reliable photometry in at least 7 filters (i.e., uncertainties  $< 0.3$  mag), we obtained best fits of sufficient quality (i.e., with sufficiently small  $\chi^2_\nu$  and  $Q > 0.001$ ) for 149 cluster candidates; we discarded the remaining 33 objects from our final sample. Of these 149 clusters, 30 were characterized by a clear IR excess, while the remaining 119 objects exhibited SEDs as expected for fully sampled clusters. We compared our derived cluster ages and masses based on application of our novel Yggdrasil-based approach (Adamo et al. 2010a,b, 2011a,b) with the results from application of GALEV+ANALYSED SED matching. The main features in the overall age and mass distributions were well reproduced by both independent approaches. Assuming a simple underlying Gaussian distribution, the peak in the age distribution resulting from our GALEV+ANALYSED analysis occurs at  $\langle \log(t \text{ yr}^{-1}) \rangle = 7.11$ , with  $\sigma_{(\log t)} = 0.80$ . For comparison, the Yggdrasil-based analysis returned  $\langle \log(t \text{ yr}^{-1}) \rangle = 7.10$ , with  $\sigma_{(\log t)} = 0.94$ . For the mass distributions, we find  $\langle \log(M_{\text{cl}}/M_\odot) \rangle = 3.38$  versus 3.37, and  $\sigma_{(\log M_{\text{cl}})} = 0.46$  versus 0.77, respectively.

The NGC 5253 cluster population is dominated by a significant number of relatively low-mass ( $M_{\text{cl}} \ll 10^5 M_\odot$ ) objects. Assuming fully sampled stellar mass functions, they have ages ranging from a few  $\times 10^6$  to a few  $\times 10^7$  yr. This age range is in excellent agreement with the starburst age of the host galaxy ( $\leq 10$  Myr). Most of our IR-excess clusters are found in the younger ‘chimney’ observed in the diagnostic age–mass plane based on our fully sampled SSP analysis, characterized by an age of  $\sim 5 \times 10^6$  yr and masses of up to a few  $\times 10^4 M_\odot$ . The observational properties of these clusters are most likely affected by a combination of stochastic sampling effects and the presence of PMS stars. The IR-excess clusters in the older chimney, at  $\log(t \text{ yr}^{-1}) = 7.1\text{--}7.2$  are also of relatively low mass and, hence, we expect them to be affected by stochastic sampling effects, while at this age the stochastic colour variations owing to luminous red stars (including RSGs) will also become apparent.

Our analysis also revealed the presence of a small number of intermediate-age ( $\sim 1$  Gyr-old),  $\sim 10^5 M_\odot$  clusters, as well as up to a dozen old clusters resembling true GCs, in relation to both their ages ( $\sim 10$  Gyr) and masses ( $\gtrsim 10^5 M_\odot$ ). Our detection of this fairly small number of true GCs is simply owing to selection effects and may not represent a genuine dearth of old, low-mass clusters in the galaxy. The presence of populations of young, intermediate-age and

old clusters supports the notion that NGC 5253 is a very active dwarf starburst galaxy that has undergone multiple episodes of star cluster formation. The steeply increasing detection limit as a function of increasing age implies that even if there were large numbers of intermediate-age and old clusters of intermediate masses, we would not be able to detect them at the present time.

## ACKNOWLEDGMENTS

We thank Angela Adamo for providing the Yggdrasil-based analysis. We also acknowledge her and Ralf Kotulla for their input in many of the technical aspects of this work. We really appreciate the referee’s useful comments and constructive suggestions leading to the final version of this manuscript. This paper is based on archival observations with the NASA/ESA *Hubble Space Telescope*, obtained from the ST-ECF archive facility. This research has also made use of NASA’s Astrophysics Data System Abstract Service. RdG and PA acknowledge research support from the National Natural Science Foundation of China (NSFC) through grant 11073001. GÖ is a Royal Swedish Academy of Sciences Research Fellow supported by a grant from the Knut and Alice Wallenberg Foundation. EZ and GÖ acknowledge financial support from the Swedish Research Council (VR) and the Swedish National Space Board.

## REFERENCES

- Adamo A., Östlin G., Zackrisson E., Hayes M., Cumming R. J., Micheva G., 2010a, MNRAS, 407, 870  
 Adamo A., Zackrisson E., Östlin G., Hayes M., 2010b, ApJ, 725, 1620  
 Adamo A., Östlin G., Zackrisson E., Hayes M., 2011a, MNRAS, 414, 1793  
 Adamo A., Östlin G., Zackrisson E., Papaderos P., Bergvall N., Rich R. M., Micheva G., 2011b, MNRAS, 415, 2388  
 Anders P., Fritze-v. Alvensleben U., 2003, A&A, 401, 1063  
 Anders P., Bissantz N., Fritze-v. Alvensleben U., de Grijs R., 2004, MNRAS, 347, 196  
 Anders P., Gieles M., de Grijs R., 2006, A&A, 451, 375  
 Annibali F., Tosi M., Aloisi A., van der Marel R. P., 2011, AJ, 142, 129  
 Barker S., de Grijs R., Cerviño M., 2008, A&A, 484, 711  
 Bastian N., Gieles M., Lamers H. J. G. L. M., Scheepmaker R. A., de Grijs R., 2005, A&A, 431, 905  
 Beck S. C., Turner J. L., Ho P. T. P., Lacy J. H., Kelly D. M., 1996, ApJ, 457, 610  
 Bellazzini M., Ferraro F. R., Pancino E., 2001, ApJ, 556, 635  
 Bellazzini M., Ferraro F. R., Sollima A., Pancino E., Origlia L., 2004, A&A, 424, 199  
 Bottinelli L., Gouguenheim L., Heidmann J., 1972, A&A, 17, 445  
 Caldwell N., Phillips M. M., 1989, ApJ, 338, 789  
 Calzetti D., Meurer G. R., Bohlin R. C., Garnett D. R., Kinney A. L., Leitherer C., Storchi-Bergmann T., 1997, AJ, 114, 1834  
 Calzetti D., Conselice C. J., Gallagher J. S., III, Kinney A. L., 1999, AJ, 118, 797  
 Calzetti D., Armus L., Bohlin R. C., Kinney A. L., Koornneef J., Storchi-Bergmann T., 2000, ApJ, 533, 682  
 Calzetti D., Harris J., Gallagher J. S., III, Smith D. A., Conselice C. J., Homeier N., Kewley L., 2004, AJ, 127, 1405  
 Campbell A., Terlevich R., Melnick J., 1986, MNRAS, 223, 811  
 Cerviño M., Luridiana V., 2004, A&A, 413, 145

- Cerviño M., Luridiana V., 2006, *A&A*, 451, 475
- Cerviño M., Luridiana V., Castander F. J., 2000, *A&A*, 360, L5
- Cerviño M., Valls-Gabaud D., Luridiana V., Mas-Hesse J. M., 2002, *A&A*, 381, 51
- Chandar R., Whitmore B. C., Calzetti D., Di Nino D., Kennicutt R. C., Regan M., Schinnerer E., 2011, *ApJ*, 727, 88
- Charlot S., 1996, in: *Proc. From Stars to Galaxies: The Impact of Stellar Physics on Galaxy Evolution*, C. Leitherer, U. Fritze-v. Alvensleben, J. Huchra, eds., *ASP Conf. Ser.*, 98, 275
- Cresci G., Vanzì L., Sauvage M., 2005, *A&A*, 433, 447
- Davidge T. J., 2007, *AJ*, 134, 1799
- de Grijs R., Fritze-v. Alvensleben U., Anders P., Gallagher J. S., Bastian N., Taylor V. A., Windhorst R. A., 2003a, *MNRAS*, 342, 259
- de Grijs R., Anders P., Bastian N., Lynds R., Lamers H. J. G. L. M., O’Neil E. J., 2003b, *MNRAS*, 343, 1285
- de Grijs R., Anders P., Lamers H. J. G. L. M., Bastian N., Fritze-v. Alvensleben U., Parmentier G., Sharina M. E., Yi S., 2005, *MNRAS*, 359, 874
- Dolphin A. E., Kennicutt R. C., Jr., 2002, *AJ*, 124, 158
- Ferland G. J., Korista K. T., Verner D. A., Ferguson J. W., Kingdon J. B., Verner E. M., 1998, *PASP*, 110, 761
- Fouesneau M., Lançon A., 2010, *A&A*, 521, A22
- Fouesneau M., Lançon A., Chandar R., Whitmore B. C., 2012, *ApJ*, 750, 60
- Freedman W. L., et al., 2001, *ApJ*, 553, 47
- Gonzalez-Riestra R., Rego M., Zamorano J., 1987, *A&A*, 186, 64
- Harbeck D., Gallagher, J., III, Crnojević, D., 2012, *MNRAS*, 422, 629
- Harris J., Calzetti D., Gallagher J. S., III, Smith D. A., Conselice C. J., 2004, *ApJ*, 603, 503
- Karachentsev I. D., et al., 2007, *AJ*, 133, 504
- Kim S. S., Morris M., Lee H. M., 1999, *ApJ*, 525, 228
- Kiss L. L., Szabó G. M., Bedding T. R., 2006, *MNRAS*, 372, 1721
- Kobulnicky H. A., Skillman E. D., 1995, *ApJ*, 454, L121
- Kobulnicky H. A., Skillman E. D., Roy J.-R., Walsh J. R., Rosa M. R., 1997, *ApJ*, 477, 679
- Kobulnicky H. A., Kennicutt R. C., Jr., Pizagno J. L., 1999, *ApJ*, 514, 544
- Kotulla R., Fritze U., Weilbacher P., Anders P., 2009, *MNRAS*, 396, 462
- Kroupa P., 2001, *MNRAS*, 322, 231
- Lampton M., Margon B., Bowyer S., 1976, *ApJ*, 208, 177
- Leitherer C., et al., 1999, *ApJS*, 123, 3
- Lejeune T., Cuisinier F., Buser R., 1997, *A&AS*, 125, 229
- Lejeune T., Cuisinier F., Buser R., 1998, *A&AS*, 130, 65
- López-Sánchez Á. R., Esteban C., 2010a, *A&A*, 516, A104
- López-Sánchez Á. R., Esteban C., 2010b, *A&A*, 517, A85
- López-Sánchez Á. R., Esteban C., García-Rojas J., Peimbert M., Rodríguez M., 2007, *ApJ*, 656, 168
- López-Sánchez Á. R., Koribalski B. S., van Eymeren J., Esteban C., Kirby E., Jerjen H., Lonsdale N., 2011, *MNRAS*, 1780
- Maíz Apellániz J., 2009, *ApSS*, 324, 95
- Marigo P., Girardi L., Bressan A., Groenewegen M. A. T., Silva L., Granato G. L., 2008, *A&A*, 482, 883
- Martin C. L., 1998, *ApJ*, 506, 222
- Martin C. L., Kennicutt R. C., Jr., 1995, *ApJ*, 447, 171
- Martín-Hernández N. L., Schaerer D., Sauvage M., 2005, *A&A*, 429, 449
- McQuinn K. B. W., et al., 2010a, *ApJ*, 721, 297
- McQuinn K. B. W., et al., 2010b, *ApJ*, 724, 49
- Meurer G. R., Heckman T. M., Leitherer C., Kinney A., Robert C., Garnett D. R., 1995, *AJ*, 110, 2665
- Meurer G. R., et al., 2006, *ApJS*, 165, 307
- Monreal-Ibero A., Vílchez J. M., Walsh J. R., Muñoz-Tuñón C., 2010, *A&A*, 517, A27
- Moorwood A. F. M., Glass I. S., 1982, *A&A*, 115, 84
- Popescu B., Hanson M. M., Elmegreen B. G., 2012, *ApJ*, 751, 122
- Press W. H., Teukolsky S. A., Vetterling W. T., Flannery B. P., 1992, *Numerical recipes in Fortran. The art of scientific computing*, 2nd ed., Cambridge: Cambridge Univ. Press
- Rieke G. H., Lebofsky M. J., Walker C. E., 1988, *ApJ*, 325, 679
- Schaerer D., Contini T., Kunth D., Meynet G., 1997, *ApJ*, 481, L75
- Schulz J., Fritze-v. Alvensleben U., Möller C. S., Fricke K. J., 2002, *A&A*, 392, 1
- Silva-Villa E., Larsen, S. S., 2010, *A&A*, 516, A10
- Silva-Villa E., Larsen, S. S., 2011, *A&A*, 529, A25
- Szczygiel D. M., Stanek K. Z., Bonanos A. Z., Pojmański G., Pilecki B., Prieto J. L., 2010, *AJ*, 140, 14
- Tremonti C. A., Calzetti D., Leitherer C., Heckman T. M., 2001, *ApJ*, 555, 322
- Turner J. L., Beck S. C., Hurt R. L., 1997, *ApJ*, 474, L11
- Turner J. L., Ho P. T. P., Beck S. C., 1998, *AJ*, 116, 1212
- Turner J. L., Beck S. C., Ho P. T. P., 2000, *ApJ*, 532, L109
- van den Bergh S., 1980, *PASP*, 92, 122
- Vanzì L., Sauvage M., 2004, *A&A*, 415, 509
- Vazquez G. A., Leitherer C., 2005, *ApJ*, 621, 695
- Walsh J. R., Roy J.-R., 1989, *MNRAS*, 239, 297
- Whitmore B. C., et al., 2011, *ApJ*, 729, 78
- Zackrisson E., Rydberg C.-E., Schaerer D., Östlin G., Tuli M., 2011 *ApJ*, 740, 13